
MAST: A Multi-fidelity Augmented Surrogate model via Spatial Trust-weighting

Ahmed Mohamed Eisa Nasr¹ Haris Moazam Sheikh¹

Abstract

In engineering design and scientific computing, computational cost and predictive accuracy are intrinsically coupled. High-fidelity simulations provide accurate predictions but at substantial computational costs, while lower-fidelity approximations offer efficiency at the expense of accuracy. Multi-fidelity surrogate modelling addresses this trade-off by combining abundant low-fidelity data with sparse high-fidelity observations. However, existing methods suffer from expensive training cost or rely on global correlation assumptions that often fail in practice to capture how fidelity relationships vary across the input space, leading to poor performance particularly under tight budget constraints. We introduce MAST, a method that blends corrected low-fidelity observations with high-fidelity predictions, trusting high-fidelity near observed samples and relying on corrected low-fidelity elsewhere. MAST achieves this through explicit discrepancy modelling and distance-based weighting with closed-form variance propagation, producing a single heteroscedastic Gaussian process. Across multi-fidelity synthetic benchmarks, MAST shows a marked improvement over the current state-of-the-art techniques. Crucially, MAST maintains robust performance across varying total budget and fidelity gaps, conditions under which competing methods exhibit significant degradation or unstable behaviour.

1. Introduction

The trade-off between predictive accuracy and computational cost is a fundamental constraint in modern simulation-based design and optimization. High-fidelity models, while necessary for precise uncertainty quantification and bias correction, are often too expensive to sample densely for

accurate surrogate construction. Conversely, low-fidelity approximations are abundant and cheap but can suffer from systematic errors that preclude their standalone use. Multi-fidelity Gaussian process (MFGP) models (Do & Zhang, 2024; Fernández-Godino, 2024; Morris, 2004; Forrester et al., 2007), bridge this gap by formalizing the correlation between data sources of varying costs. By supplementing sparse high-fidelity data with abundant low-fidelity observations, MFGP models paint a more accurate picture of the underlying response surface at a fraction of the computational budget required by high-fidelity-only approaches (Perdikaris et al., 2015).

The key assumption underlying multi-fidelity methods is that lower-fidelity models, while imperfect, capture dominant trends of the true function, allowing limited high-fidelity data to correct residual discrepancies. Existing approaches encode this through *global correlation structures*. Autoregressive models (Kennedy & O’hagan, 2000; Le Gratiet & Garnier, 2014) assume linear inter-fidelity relationships that must hold across the input domain; multi-output formulations (Alvarez et al., 2012) impose separable covariance structures implying spatially constant correlations; and fidelity-augmented kernel methods (Poloczek et al., 2017; Wu et al., 2020) learn global kernel parameters that must extrapolate from sparse high-fidelity data. However, when the inter-fidelity relationships vary spatially, these assumptions can break down, leading to model misspecification and degraded predictive performance. More expressive approaches, nonlinear autoregressive GPs (Perdikaris et al., 2017) and deep multi-fidelity GPs (Cutajar et al., 2019), can capture complex inter-fidelity mappings but require more training data and careful hyperparameters tuning (Brevault et al., 2020), often unavailable under tight budget constraints. Fusion-based methods (Lam et al., 2015; Thomison & Allaire, 2017) avoid hierarchical assumptions by combining independent per-fidelity surrogates, yet perform fusion at the distributional level without exploiting geometric proximity between fidelity samples.

We introduce **MAST** (*Multi-fidelity Augmented Surrogate model with Trust-region weighting*), which replaces classical correlation learning with a *geometric inductive bias*. The core insight is simple: corrected low-fidelity observations should be trusted far from high-fidelity samples where no calibration information exists, but should progressively

¹Department of Aeronautics and Astronautics, University of Southampton, Southampton, United Kingdom. Correspondence to: Haris Moazam Sheikh <H.M.Sheikh@soton.ac.uk>.

yield to high-fidelity predictions as high-fidelity data becomes available *nearby*. MAST operationalizes this principle through explicit discrepancy modelling followed by distance-based, cost-aware weighted fusion of corrected low-fidelity values with high-fidelity posterior predictions. The uncertainty induced by both discrepancy estimation and spatial blending is analytically propagated into fixed heteroscedastic noise terms, yielding a single Gaussian process surrogate that naturally down-weights unreliable data through geometric proximity rather than learned correlation structures. Our contributions can be summarized as:

1. A geometrically driven augmentation scheme that adapts inter-fidelity fusion locally without parametric correlation assumptions.
2. Explicit incorporation of fidelity cost into trust weighting, establishing an economic hierarchy that governs information fusion.
3. Closed-form variance propagation enabling efficient single-GP training while avoiding optimization instabilities of learned heteroscedastic models.
4. State-of-the-art predictive accuracy and uncertainty calibration across several benchmarks.
5. Robust performance across budget allocations, total budget scales, and inter-fidelity correlation levels.

The remainder of this paper is organized as follows. Section 2 surveys related work. Section 3 reviews Gaussian process fundamentals. Section 5 presents synthetic experiments setup. Section 4 presents the MAST framework. Section 6 reports experimental results. Section 7 concludes.

2. Related Work

Multi-fidelity surrogate modelling has been studied extensively across statistics, machine learning, and engineering design (Fernández-Godino, 2024; Perdikaris et al., 2015; Wang et al., 2023). Existing approaches can be broadly categorized according to how inter-fidelity relationships are modelled and exploited.

Linear Autoregressive Models. The foundational framework for multi-fidelity GP modelling was introduced by Kennedy & O’hagan (2000), who proposed an autoregressive (AR1) co-kriging model relating adjacent fidelity levels via

$$f^{(s)}(\mathbf{x}) = \rho_s f^{(s-1)}(\mathbf{x}) + \delta^{(s)}(\mathbf{x}), \quad (1)$$

where ρ_s is a scalar correlation parameter and $\delta^{(s)}(\mathbf{x}) \sim \mathcal{GP}(0, k_\delta^{(s)})$ is an independent discrepancy process. This formulation was later simplified by Han & Görtz (2012) and generalized to multiple fidelity levels through recursive co-kriging (Le Gratiet & Garnier, 2014). Forrester

et al. (2007) developed comprehensive framework for multi-fidelity optimization. Gradient-enhanced variants incorporating derivative information have also been developed (Chung & Alonso, 2002; Leary et al., 2004) and more recently by Han et al. (2013). These autoregressive methods have been successfully applied across diverse engineering domains (Matar et al., 2025; Ding & Kareem, 2018; Liu et al., 2022; Wiegand et al., 2025; Toal & Keane, 2011; Laurenceau & Sagaut, 2008; Keane, 2012). A key limitation is the requirement for nested sampling designs where high-fidelity locations must be a subset of low-fidelity locations, precluding independent optimization of sampling at each fidelity level (Wang et al., 2023). Furthermore, the global correlation parameter ρ_s assumes a spatially constant inter-fidelity relationship, which breaks down when discrepancies vary across the input domain (Brevault et al., 2020).

Nonlinear and Deep Multi-Fidelity Models. To relax linear correlation assumptions, Perdikaris et al. (2017) proposed nonlinear autoregressive Gaussian processes (NARGP), replacing the linear scaling in Eq. (1) with a nonlinear mapping: $f^{(s)}(\mathbf{x}) = g^{(s)}(\mathbf{x}, f^{(s-1)}(\mathbf{x}))$, where $g^{(s)}$ is modelled as a GP over the augmented input space. However, NARGP employs a disjointed hierarchical architecture: each fidelity-level GP is fitted in isolation, and lower-fidelity models remain fixed once trained. This greedy layer-wise approach prevents information from higher fidelities from refining lower-fidelity representations. To address this limitation, Cutajar et al. (2019) proposed deep multi-fidelity Gaussian processes (MF-DGP), extending NARGP to a fully coupled deep GP architecture where all layers are trained jointly. However, the composition of GP layers renders the posterior non-Gaussian, necessitating approximate inference techniques that increase computational complexity. Furthermore, the number of hyperparameters grows with network depth, and empirical studies suggest these models may underperform simpler baselines in data-scarce regimes where insufficient data precludes reliable hyperparameter estimation (Brevault et al., 2020; Do & Zhang, 2024).

Multi-Output and Multi-Task Gaussian Processes. An alternative perspective treats fidelities as correlated outputs within a multi-output or multi-task GP framework. Coregionalization models such as LMC and ICM express inter-fidelity correlations via shared latent processes (Alvarez et al., 2012). These formulations enable flexible information sharing across fidelities and have been applied successfully in optimization tasks (Toal, 2023; Mikkola et al., 2023; Poloczek et al., 2017; Brevault et al., 2020; Takeno et al., 2020). However, they typically assume separable covariance structures, implying spatially constant cross-fidelity correlations across the input domain, and learning the inter-task correlation explicitly can be computationally expensive or numerically unstable (Alvarez & Lawrence, 2011; Alvarez et al., 2012; Liu et al., 2018).

Specialized Kernels Models. Within Bayesian optimization, several approaches incorporate fidelity through specialized kernels or augmented input spaces. These include multi-information source optimization kernels (Poloczek et al., 2017), fidelity-augmented Gaussian processes (Kandasamy et al., 2017; Wu et al., 2020), additive latent-function constructions (Song et al., 2019). While effective in optimization settings, these methods generally rely on globally learned kernel structures that must extrapolate from sparse high-fidelity data, limiting their ability to adapt fidelity relationships or uncertainty estimates in regions poorly supported by data (Kandasamy et al., 2017).

Fusion-Based and Reliability-Aware Methods. Fusion-based approaches relax the assumption of a strict fidelity hierarchy by combining independent surrogates. Lam et al. (2015) construct independent GP surrogates for each source and fuse them via precision-weighted averaging. Thomison & Allaire (2017) further remove hierarchical assumptions by estimating cross-model error correlations through a model reification procedure, allowing correlation-aware fusion without requiring paired observations or nested designs. Related reliability-aware formulations treat fidelity differences as source-dependent uncertainty within a unified probabilistic model (Ghoreishi & Allaire, 2018; Fan et al., 2024). While these approaches successfully eliminate hierarchy constraints and allow non-nested information sources, fusion is typically performed at the distributional level and does not explicitly exploit geometric proximity between fidelity samples when calibrating local discrepancies.

In our empirical evaluation, we benchmark MAST against representative methods from each category: the autoregressive co-kriging model (Kennedy & O’hagan, 2000), recursive co-kriging (Le Gratiet & Garnier, 2014), multi-information source surrogate modelling via precision-weighted fusion (Lam et al., 2015), model reification-based fusion (Thomison & Allaire, 2017), nonlinear autoregressive Gaussian processes (NARGP) (Perdikaris et al., 2017), deep multi-fidelity Gaussian processes (MF-DGP) (Cutajar et al., 2019), and BoTorch SingleTaskMultiFidelityGP using Specialized kernels (Poloczek et al., 2017; Wu et al., 2020).

3. Background

3.1. Gaussian Process Regression

Gaussian process (GP) is defined as a collection of random variables, any finite subset of which follows a joint Gaussian distribution (Rasmussen & Williams, 2006). A real-valued function $f(\mathbf{x})$ is said to follow a Gaussian process,

$$f(\mathbf{x}) \sim \mathcal{GP}(m(\mathbf{x}), k(\mathbf{x}, \mathbf{x}')), \quad (2)$$

where $m(\mathbf{x}) = \mathbb{E}[f(\mathbf{x})]$ is the mean function and $k(\mathbf{x}, \mathbf{x}')$ is a positive semi-definite covariance kernel encoding prior

assumptions about smoothness and correlation structure.

Given noisy observations $\mathcal{D} = \{(\mathbf{x}_i, y_i)\}_{i=1}^N$ with $y_i = f(\mathbf{x}_i) + \varepsilon_i$, and $\varepsilon_i \sim \mathcal{N}(0, \sigma^2)$, the GP posterior at a test input \mathbf{x}_* is Gaussian, $p(f(\mathbf{x}_*) | \mathcal{D}) = \mathcal{N}(\mu(\mathbf{x}_*), \sigma^2(\mathbf{x}_*))$, with predictive mean and variance given by

$$\mu(\mathbf{x}_*) = \mathbf{k}_*^\top (\mathbf{K} + \sigma^2 \mathbf{I})^{-1} \mathbf{y}, \quad (3)$$

$$\sigma^2(\mathbf{x}_*) = k(\mathbf{x}_*, \mathbf{x}_*) - \mathbf{k}_*^\top (\mathbf{K} + \sigma^2 \mathbf{I})^{-1} \mathbf{k}_*, \quad (4)$$

where \mathbf{K} is the kernel matrix evaluated at the training inputs and \mathbf{k}_* is the vector of cross-covariances between \mathbf{x}_* and the training set.

3.2. Multi-fidelity Problem Setting

We consider a budget-constrained multi-fidelity setting with M fidelity levels indexed by $m \in \{1, \dots, M\}$, where $m = M$ denotes the highest fidelity. High-fidelity data is assumed to be sparse due to its high evaluation cost, while lower-fidelity observations are more abundant. Evaluation costs satisfy $\mathcal{C}_1 < \mathcal{C}_2 < \dots < \mathcal{C}_M$, establishing an economic hierarchy where higher indices correspond to more expensive (and typically more accurate) fidelity levels. Given a computational budget \mathcal{B} , we collect observations at each fidelity level such that:

$$\mathcal{D}_m = \{(\mathbf{x}_i^{(m)}, y_i^{(m)})\}_{i=1}^{N_m}, \quad m = 1, \dots, M, \quad (5)$$

where $y_i^{(m)} = f_m(\mathbf{x}_i^{(m)}) + \epsilon_i^{(m)}$ with Gaussian observation noise $\epsilon_i^{(m)} \sim \mathcal{N}(0, \sigma_m^2)$. The goal is to construct a surrogate model that accurately approximates the highest-fidelity function $f_M(\mathbf{x})$ by leveraging all data sources.

4. MAST Framework

The MAST framework is built on a simple geometric intuition: the reliability of a corrected low-fidelity observation depends on how close it is to high-fidelity calibration data. Near high-fidelity samples, we have direct evidence of the discrepancy between fidelities, so corrections are well-grounded. Far from high-fidelity samples, corrections are extrapolated and less certain—but the corrected low-fidelity value remains the best available estimate in that region. MAST implements this through a three-stage procedure: independent GP training, discrepancy-based correction with spatially-weighted blending, and heteroscedastic GP fusion.

4.1. Algorithmic Summary

Algorithm 1 summarizes the complete MAST procedure for the general M -fidelity case. A more detailed explanation can be found in Appendix C.

4.1.1. STAGE 1: INDEPENDENT BASELINE MODELLING

We first train independent GPs for each fidelity level to capture their intrinsic characteristics and noise levels. A GP prior is placed on each function $f_m \sim \mathcal{GP}(0, k_m)$ for $m \in \{1, \dots, M\}$, utilizing an RBF kernel. The hyperparameters $\{\ell_m, \sigma_{f,m}^2\}$ and the observation noise variances σ_m^2 are estimated via Type-II Maximum Likelihood Estimation (MLE). The learned noise levels $\hat{\sigma}_m$ serve as estimates of the intrinsic uncertainty at each fidelity.

4.1.2. STAGE 2: DISCREPANCY MODELLING AND SPATIALLY-WEIGHTED AUGMENTATION

The central contribution of MAST is the augmentation scheme that first corrects each lower-fidelity observation using a learned discrepancy function, then blends the corrected value with the high-fidelity GP prediction using spatially-adaptive weights. For each fidelity level $m < M$, the procedure transforms \mathcal{D}_m into an augmented dataset $\tilde{\mathcal{D}}_m$.

Discrepancy modelling. We model the discrepancy between fidelity level m and the highest fidelity M by fitting a GP. We compute residuals at the high-fidelity observation locations:

$$\delta_m(\mathbf{x}_j^{(M)}) = y_j^{(M)} - \mu_m(\mathbf{x}_j^{(M)}), \quad j = 1, \dots, N_M, \quad (6)$$

where $\mu_m(\cdot)$ is the posterior mean of the fidelity- m GP. We then fit a Gaussian process \mathcal{GP}_{δ_m} to these residuals, obtaining the posterior mean $\mu_{\delta_m}(\cdot)$ and variance $\sigma_{\delta_m}^2(\cdot)$ at any location. Using the trained high-fidelity GP, we also obtain the posterior mean $\mu_M(\mathbf{x}_i^{(m)})$ and variance $\sigma_M^2(\mathbf{x}_i^{(m)})$ at each fidelity- m input location.

Spatially-adaptive weighting. For each low-fidelity point $\mathbf{x}_i^{(m)}$, we compute a weight that determines the relative contribution of the corrected low-fidelity value versus the high-fidelity GP prediction. This weight should depend on the spatial proximity to high-fidelity observations: points near high-fidelity samples should favour high-fidelity predictions, while points far from high-fidelity samples should favour corrected low-fidelity values.

We first compute the Euclidean distance from $\mathbf{x}_i^{(m)}$ to each high-fidelity point in the normalized input space:

$$d_{ij} = \|\tilde{\mathbf{x}}_i^{(m)} - \tilde{\mathbf{x}}_j^{(M)}\|_2, \quad j = 1, \dots, N_M. \quad (7)$$

A naive approach would aggregate contributions from all high-fidelity points, but this leads to problematic behaviour: a low-fidelity point with a nearby high-fidelity neighbour would still be influenced by distant high-fidelity observations elsewhere in the domain. To ensure that only *locally relevant* high-fidelity information contributes, we introduce an adaptive trust region based on an N -sphere centred at

$\mathbf{x}_i^{(m)}$. The radius of this trust region should scale with the distance to the nearest high-fidelity point, i.e., $r_i = g(d_{\min})$. In principle, any monotonically increasing function g could be used; we adopt:

$$r_i = \sqrt{d_{\min}}, \quad \text{where } d_{\min} = \min_j d_{ij}, \quad (8)$$

which we found empirically to provide robust performance. Only high-fidelity points within this N -sphere contribute to the weight computation: $\mathcal{N}_i = \{j : d_{ij} \leq r_i\}$.

For each high-fidelity point $j \in \mathcal{N}_i$, we compute a distance-based weight:

$$w_j = 1 - d_{ij}^{\alpha_m}, \quad \text{where } \alpha_m = \frac{\log_{10}(\mathcal{C}_M/\mathcal{C}_m)}{2}. \quad (9)$$

The exponent α_m controls how quickly the weight decays with distance. Critically, α_m encodes the fidelity hierarchy, determining how much spatial influence each fidelity level exerts. In principle, α_m can be derived from any quantity that establishes an ordering among fidelities: evaluation cost ratios, user-specified confidence levels, known approximation orders, or domain expertise. In this work, we define α_m as a function of the fidelity cost ratio $\mathcal{C}_M/\mathcal{C}_m$, explicitly incorporating evaluation cost into the weighting scheme. Alternative weight functions are also possible (e.g., exponential decay) provided $w_j = g(d_{ij}; \alpha_m)$ where $g(\cdot)$ is monotonically decreasing in distance; we found the form in Eq. (9) to work well empirically.

The individual weights are aggregated into a single low-fidelity weight $W_m^{(i)}$ for each point $\mathbf{x}_i^{(m)}$:

$$W_m^{(i)} = 1 - \frac{1}{|\mathcal{N}_i|} \sum_{j \in \mathcal{N}_i} w_j, \quad (10)$$

By construction, $W_m^{(i)}$ decreases as proximity to high-fidelity observations increases. This locality mechanism ensures that only nearby high-fidelity observations influence the weighting.

Augmented observations: Each low-fidelity observation is corrected by adding the predicted discrepancy, then blended with the high-fidelity GP prediction, with the low-fidelity weight $W_m^{(i)}$ determining the contribution of each component:

$$\tilde{y}_i^{(m)} = W_m^{(i)} \cdot \left(y_i^{(m)} + \mu_{\delta_m}(x_i^{(m)}) \right) + (1 - W_m^{(i)}) \cdot \mu_M(x_i^{(m)}). \quad (11)$$

Variance of augmented observations: The augmented observation $\tilde{y}_i^{(m)}$ is a weighted sum of two independent quantities, each contributing uncertainty to the augmented

Algorithm 1 MAST: Multi-fidelity Augmented Surrogate with Trust-region Weighting

Require: Data $\{\mathcal{D}_m\}_{m=1}^M$; Cost ratios $C_m = \mathcal{C}_M/\mathcal{C}_m$

Ensure: Trained surrogate model \mathcal{M}

- 1: **Stage 1:** Train independent \mathcal{GP}_m on each $\mathcal{D}_m \rightarrow$ obtain $\hat{\sigma}_m$
- 2: **Stage 2:** For each fidelity $m < M$:
- 3: Compute residuals $\delta_j = y_j^{(M)} - \mu_m(\mathbf{x}_j^{(M)})$ at HF locations
- 4: Fit discrepancy \mathcal{GP}_{δ_m} to residuals
- 5: For each point $\mathbf{x}_i^{(m)}$:
- 6: Compute local trust region \mathcal{N}_i and weight $W_m^{(i)}$
- 7: Augment observations: \tilde{y}_i via Eq (11)
- 8: Propagate variance: $\tilde{\sigma}_i^2$ via Eq. (12)
- 9: **Stage 3:** Train final \mathcal{GP} on \mathcal{D}_{aug} with fixed per-point variances
- 10: **return** $\mathcal{M} \leftarrow \mathcal{GP}$

observation. Since these two components are independent, the total variance follows from standard propagation rules:

$$\tilde{\sigma}_i^2 = \left(W_m^{(i)}\right)^2 \left(\hat{\sigma}_m^2 + \sigma_{\delta_m}^2(\mathbf{x}_i^{(m)})\right) + \left(1 - W_m^{(i)}\right)^2 \sigma_M^2(\mathbf{x}_i^{(m)}). \quad (12)$$

This formulation ensures that augmented points near high-fidelity data (where $W_m^{(i)} \rightarrow 0$) inherit the lower uncertainty of high-fidelity predictions, while points far from high-fidelity observations (where $W_m^{(i)} \rightarrow 1$) retain the combined uncertainty of the original measurement and discrepancy estimation.

4.1.3. STAGE 3: GAUSSIAN PROCESS FUSION WITH FIXED OBSERVATION VARIANCES

The final surrogate is trained on the combined dataset consisting of original high-fidelity observations and augmented lower-fidelity observations from all levels:

$$\mathcal{D}_{\text{aug}} = \left\{ \left(\mathbf{x}_j^{(M)}, y_j^{(M)}, \hat{\sigma}_M^2 \right) \right\}_{j=1}^{N_M} \bigcup_{m=1}^{M-1} \left\{ \left(\mathbf{x}_i^{(m)}, \tilde{y}_i^{(m)}, \tilde{\sigma}_i^2 \right) \right\}_{i=1}^{N_m}. \quad (13)$$

We fit a Gaussian process where each observation has a *fixed*, pre-computed noise variance. These observation variances are *not learned* during GP training; they remain fixed at the values computed in Stage 2. This allows the GP to weight observations according to their pre-determined reliability, naturally down-weighting uncertain augmented points while trusting high-fidelity observations.

5. Synthetic Experiments

To enable fair and consistent comparison with established multi-fidelity surrogate models, we define standardized

benchmarking configurations for both two-fidelity and three-fidelity scenarios. These configurations are shared across all methods and problem instances to isolate surrogate modelling performance under controlled computational budgets.

Experiments are conducted on a suite of standard benchmark functions spanning low- to high-dimensional settings, with each function defined over its canonical domain $\mathbf{x} \in [\mathbf{x}_{\min}, \mathbf{x}_{\max}]^d$. All functions exhibit spatially-varying discrepancy between fidelity levels, except Ackley and Park2.

To systematically control inter-fidelity correlation, we adopt a degradation-based formulation in which the low-fidelity function is defined as:

$$f_{LF}(\mathbf{x}) = f_{HF}(\mathbf{x}) + d \cdot \delta(\mathbf{x}), \quad (14)$$

where $f_{HF}(\mathbf{x})$ is the high-fidelity function, $\delta(\mathbf{x})$ is a function-specific deviation term, and $d \geq 0$ governs the severity of the fidelity discrepancy. This construction preserves realistic bias structures while allowing controlled variation of inter-fidelity dependence.

For each test function and budget configuration, 25 independent experimental repetitions were conducted with different random seeds to ensure statistical robustness. Training points are sampled using Latin Hypercube Sampling (LHS) to ensure space-filling coverage of the design space. Model evaluation is performed on a fixed set of test points per function. All Gaussian process models employ squared exponential (RBF) kernels with automatic relevance determination (ARD), and hyperparameters are optimized using maximum likelihood estimation via BoTorch (Balandat et al., 2020), with the exception of NARGP and MF-DGP that use their respective open-source repositories. Results are reported as mean normalized by cost-equivalent HF-only results.

The total computational budget is defined as $\mathcal{B} = 5D$, measured in equivalent high-fidelity evaluations. Fidelity costs are fixed across all experiments following (Vaiuso et al., 2025), with $\mathcal{C}_{HF} = 1.0$, $\mathcal{C}_{MF} = 0.2$, and $\mathcal{C}_{LF} = 0.1$. Budget allocation is determined via cost-based splits. The total evaluation budget is allocated across fidelity levels using fixed cost-based splits: 70%/30% (HF/LF) for two-fidelity experiments and 50%/30%/20% (HF/MF/LF) for three-fidelity experiments. The number of samples at fidelity level m is computed as $N_m = \frac{\gamma_m \mathcal{B}}{\mathcal{C}_m}$, where γ_m denotes the budget fraction assigned to fidelity m and \mathcal{C}_m is the cost of a single evaluation at fidelity m .

The surrogate models performance is evaluated using two complementary metrics: Predictive accuracy is quantified using the root mean square error (RMSE),

$$\text{RMSE} = \sqrt{\frac{1}{N_{\text{test}}} \sum_{i=1}^{N_{\text{test}}} (\mu(x_i) - f_M(x_i))^2}, \quad (15)$$

while uncertainty calibration is assessed via the mean probability density function (mean PDF),

$$\text{mean PDF} = \frac{1}{N_{\text{test}}} \sum_{i=1}^{N_{\text{test}}} \mathcal{N}(f_M(x_i) \mid \mu(x_i), \sigma^2(x_i)). \tag{16}$$

While RMSE is conventionally used for evaluating model performance, we believe for Gaussian processes, mean PDF is the more meaningful metric as it evaluates both predictive accuracy and uncertainty calibration. Here, $\mu(x_i)$ and $\sigma^2(x_i)$ denote the surrogate model’s predictive mean and variance at test input x_i , and $f_M(x_i)$ denotes the corresponding ground-truth function value.

6. Results

6.1. Two-Fidelity Results

Table 1 presents the normalized performance across ten benchmark functions spanning 2 to 10 input dimensions, where RMSE values below unity and mean PDF values above unity indicate improvement over the HF-only baseline. MAST achieves the best RMSE on 7 of 10 functions and the best Mean PDF on 5 of 10 functions, demonstrating consistent performance across diverse problem landscapes. On functions where MAST does not achieve the best result, it remains competitive, for instance, on Hartmann3 and Park2 where AR1 excels due to strong global linear correlation, MAST still achieves meaningful improvements.

Among competitors, AR1 co-kriging performs well on low-dimensional problems where inter-fidelity correlation is spatially constant (e.g., Hartmann3, Park2) but degrades sharply otherwise. BoTorch MF-GP shows consistent modest improvements on smooth functions (best on Hartmann6). The deep learning approaches (NARGP, MF-DGP) consistently underperform, with MF-DGP showing catastrophic uncertainty miscalibration on Borehole, suggesting insufficient data under budget constraints ($\mathcal{B} = 5D$).

6.2. Three-Fidelity Results

Table 2 presents the performance for the three-fidelity configuration, where an intermediate mid-fidelity level (with $d = 0.5$ in Eq 17) bridges low- and high-fidelity sources.

MAST achieves the best RMSE on 7 of 10 functions and the best Mean PDF on 7 of 10 functions. Performance is consistent with the two-fidelity case, demonstrating that MAST’s augmentation strategy effectively incorporates additional fidelity levels without loss of robustness. For all test functions where MAST is not best, it maintains competitive performance. Methods relying on strict hierarchical assumptions continue to struggle on multimodal and higher-dimensional problems, while BoTorch retains competitive performance primarily on low-dimensional smooth functions. Although

MF-DGP shows isolated improvements in RMSE, its uncertainty calibration remains unreliable under the available budget.

6.3. Sensitivity to Budget Allocation

To assess robustness to budget allocation choices, the HF cost fraction was varied while keeping total budget fixed at $\mathcal{B} = 5D$. Figure 1 shows normalized performance across three representative functions. MAST maintains consistently strong performance across the entire allocation range across all benchmarks regardless of the proportion of budget allocated to high-fidelity evaluations, representing a significant error reduction. This stability contrasts sharply with competing methods: AR1 exhibits erratic behaviour, while NARGP and MF-DGP consistently underperform the baseline. Notably, at HF fraction = 0.1, MAST still achieves substantial improvements—other methods either degrade significantly or become unstable in this low-HF regime. The uncertainty quantification results are striking: MAST’s mean PDF maintain consistent and stable performance compared to other methods. These results suggest that MAST is robust to any allocation decisions compared to competing methods.

6.4. Sensitivity to Total Budget

To evaluate scaling with computational resources, total budget was varied from $0.25 \times$ to $3.0 \times$ the base budget $\mathcal{B} = 5D$, maintaining fixed 70%/30% cost split. Figure 2 shows normalized performance as budget scales. MAST demonstrates stable performance regardless of budget scale, maintaining a robust performance across benchmarks, particularly in data-scarce regimes. Several baselines exhibit problematic scaling: AR1 shows high variance across budgets, while MF-DGP remains at $2 \times$ worse than baseline throughout. Data-hungry methods (NARGP, MF-DGP) improve with increased budget on Rastrigin but even at $3 \times$ budget fail to match MAST’s performance at $0.25 \times$ budget. MAST also provides exceptional uncertainty calibration, while competing methods cluster near or below baseline. This underscores MAST’s suitability for budget-constrained applications where data scarcity renders competing methods.

6.5. Sensitivity to Fidelity Discrepancy

To assess the robustness of varying inter-fidelity correlation, the degradation parameter d (function of cost) in Equation (17) was swept from 0.25 (high correlation, high cost) to 2.0 (low correlation, low cost). Figure 3 shows normalized performance across three functions. MAST maintains strong performance across the entire range of fidelity discrepancies. MAST achieves RMSE reduction consistently, while most competing methods hover near or above baseline regardless of correlation level. AR1 shows degradation with

Table 1. Surrogate model performance comparison. All values are normalized relative to the HF-only baseline. For RMSE, values < 1 indicate improvement. For Mean PDF, values > 1 indicate improvement. Best results per function and metric are highlighted in **bold**.

Test Function	Normalized RMSE ↓								Normalized Mean PDF ↑							
	MAST	ARI	Recur.	Reif.	BoTorch	NARGP	MF-DGP	MISO	MAST	ARI	Recur.	Reif.	BoTorch	NARGP	MF-DGP	MISO
Branin (2D)	0.63	1.08	1.38	1.35	0.82	1.14	1.49	1.34	3.60	1.83	2.87	4.19	1.20	1.65	2.69	4.14
Hartmann3 (3D)	0.64	0.26	1.22	0.39	0.27	0.47	0.89	0.40	1.69	3.71	0.73	2.39	2.37	2.43	0.88	2.23
Ackley (4D)	0.64	1.25	0.99	0.98	1.01	1.08	1.23	0.92	1.89	1.35	0.91	1.14	0.94	1.13	0.93	1.18
Park1 (4D)	0.93	1.03	4.37	2.28	0.98	1.08	2.75	2.14	1.30	1.37	0.47	0.37	0.72	1.34	0.26	0.42
Park2 (4D)	0.67	0.34	1.40	2.76	0.49	1.27	1.31	2.68	1.55	2.97	0.66	0.13	1.26	0.91	0.65	0.11
Rastrigin (5D)	0.95	2.56	1.01	1.03	1.00	2.61	2.49	0.99	1.35	0.99	0.99	1.04	1.04	0.60	0.64	1.15
Hartmann6 (6D)	0.80	0.70	0.99	0.83	0.63	0.90	1.08	0.80	1.25	1.43	1.04	1.35	1.11	1.23	0.84	1.38
Levy (7D)	0.88	2.30	1.01	1.01	1.00	2.30	2.23	1.00	1.58	0.24	1.02	1.12	1.06	0.41	0.15	1.17
Borehole (8D)	0.07	1.97	1.00	1.14	1.04	1.97	1.97	1.02	29.94	0.23	1.00	1.15	1.13	0.50	0.03	1.20
Rosenbrock (10D)	0.50	5.05	1.00	1.00	1.00	2.06	2.06	1.00	2.66	0.14	1.01	1.09	1.05	0.47	0.13	1.16

Table 2. Surrogate model performance for the three-fidelity configuration. All values are normalized relative to the HF-only baseline. For RMSE, values < 1 indicate improvement. For Mean PDF, values > 1 indicate improvement. Best results per function and metric are highlighted in **bold**.

Test Function	Normalized RMSE ↓								Normalized Mean PDF ↑							
	MAST	ARI	Recur.	Reif.	BoTorch	NARGP	MF-DGP	MISO	MAST	ARI	Recur.	Reif.	BoTorch	NARGP	MF-DGP	MISO
Branin (2D)	0.62	1.25	4.23	1.11	0.70	1.33	0.67	1.02	3.45	1.42	1.29	2.24	1.45	0.86	3.28	2.41
Hartmann3 (3D)	0.69	0.51	1.02	2.67	0.29	0.92	0.91	0.55	1.44	2.16	0.83	1.55	2.19	1.24	0.61	1.78
Ackley (4D)	0.66	1.54	1.02	1.08	1.02	0.88	1.26	0.97	1.72	1.15	0.79	1.18	1.01	1.34	0.90	1.22
Park1 (4D)	1.04	1.08	1.98	4.00	1.15	1.46	2.07	1.69	1.17	1.08	0.59	0.47	0.60	0.90	0.23	0.53
Park2 (4D)	0.78	0.62	0.90	2.36	0.60	1.06	1.28	2.38	1.26	1.80	1.06	0.21	1.08	1.17	0.43	0.13
Rastrigin (5D)	0.98	3.85	1.02	1.03	1.01	2.03	1.90	0.99	1.30	0.68	0.97	1.17	1.09	0.77	0.80	1.21
Hartmann6 (6D)	0.87	0.92	0.98	2.06	0.64	1.18	1.21	0.84	1.24	1.26	1.06	1.23	1.14	1.02	0.80	1.45
Levy (7D)	0.87	2.24	1.01	1.03	1.00	2.30	2.25	1.00	1.56	0.47	0.99	1.16	1.09	0.41	0.09	1.21
Borehole (8D)	0.07	1.97	1.00	1.08	1.02	1.97	1.97	1.02	27.50	0.47	1.01	1.01	1.14	0.50	0.03	1.22
Rosenbrock (10D)	0.49	3.40	1.01	1.00	1.00	2.06	2.06	1.00	2.67	0.16	1.00	1.16	1.09	0.49	0.33	1.21

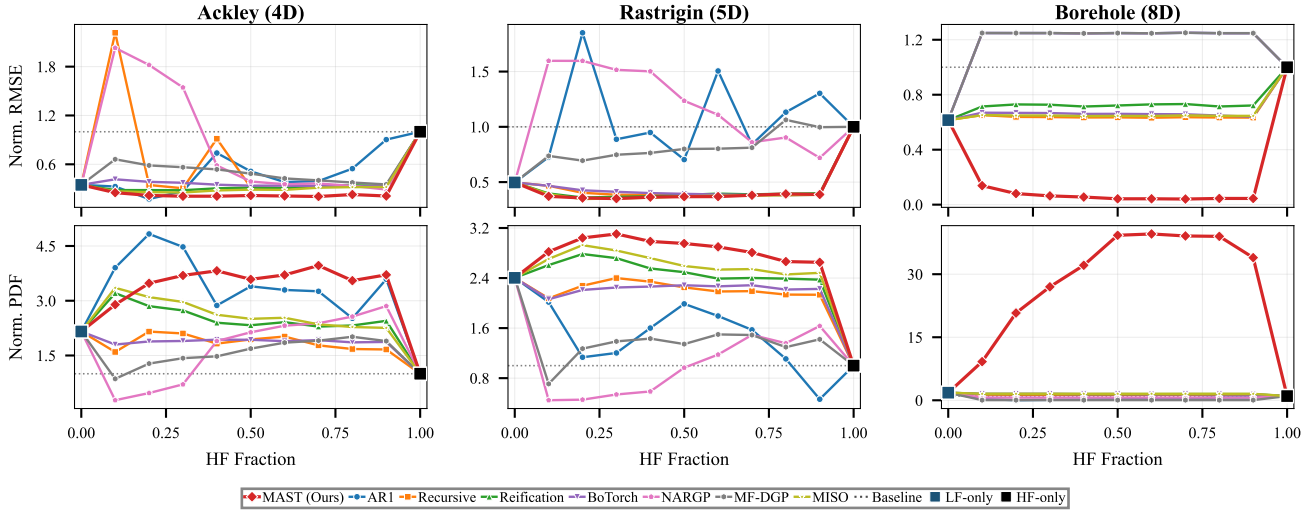


Figure 1. Sensitivity of surrogate model performance to budget allocation. The HF fraction represents the proportion of total budget $B = 5D$ allocated to high-fidelity evaluations, with the remainder spent on low-fidelity samples. Top row: Normalized RMSE; bottom row: Normalized Mean PDF. All values are normalized relative to the HF-only baseline (dotted line at 1.0). Square markers indicate single-fidelity baselines: LF-only (navy) and HF-only (black).

increasing discrepancy on two benchmarks, eventually performing worse than baseline. The uncertainty quantification results are particularly notable, MAST achieves better mean PDF than baseline across all discrepancy levels and benchmarks, adapting naturally as the relative fidelity gap changes. MAST achieves this robustness by explicitly encoding the fidelity gap through its cost-aware weighting exponent, rather

than learning correlations that may not generalize.

7. Discussion and Conclusion

The results indicate that spatial locality is a more reliable inductive bias than learned correlation structures for multi-fidelity surrogate modelling in data-scarce regimes. By

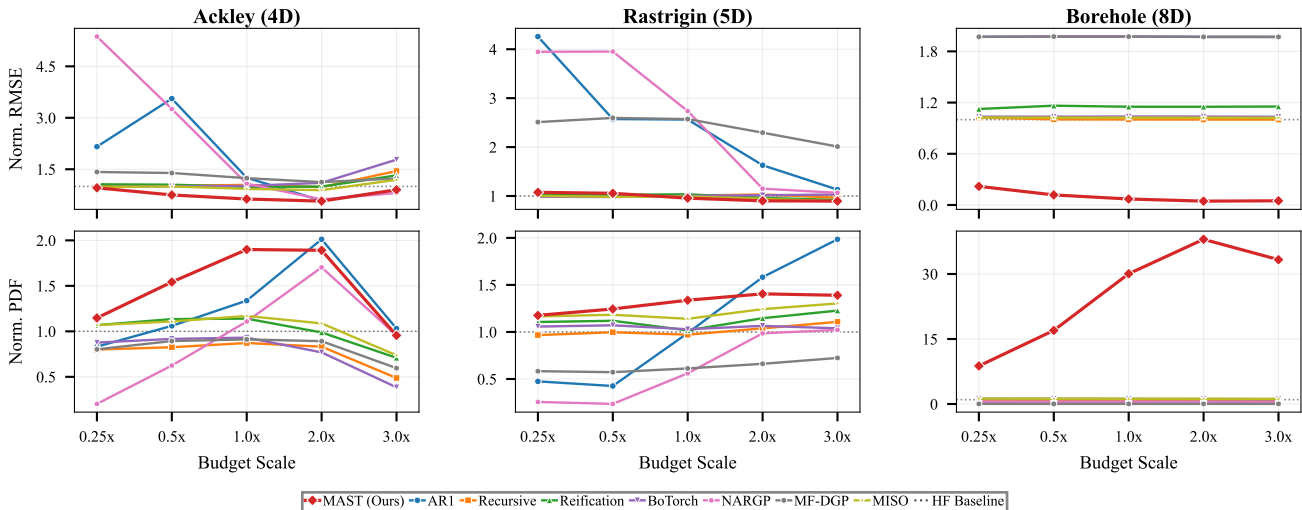


Figure 2. Sensitivity of surrogate model performance to total computational budget. Budget scale is relative to the base budget $\mathcal{B} = 5D$, with fixed 70%/30% HF/LF cost allocation. Top row: Normalized RMSE (lower is better); bottom row: Normalized Mean PDF (higher is better). All values are normalized relative to the HF-only baseline at each budget level (dotted line at 1.0).

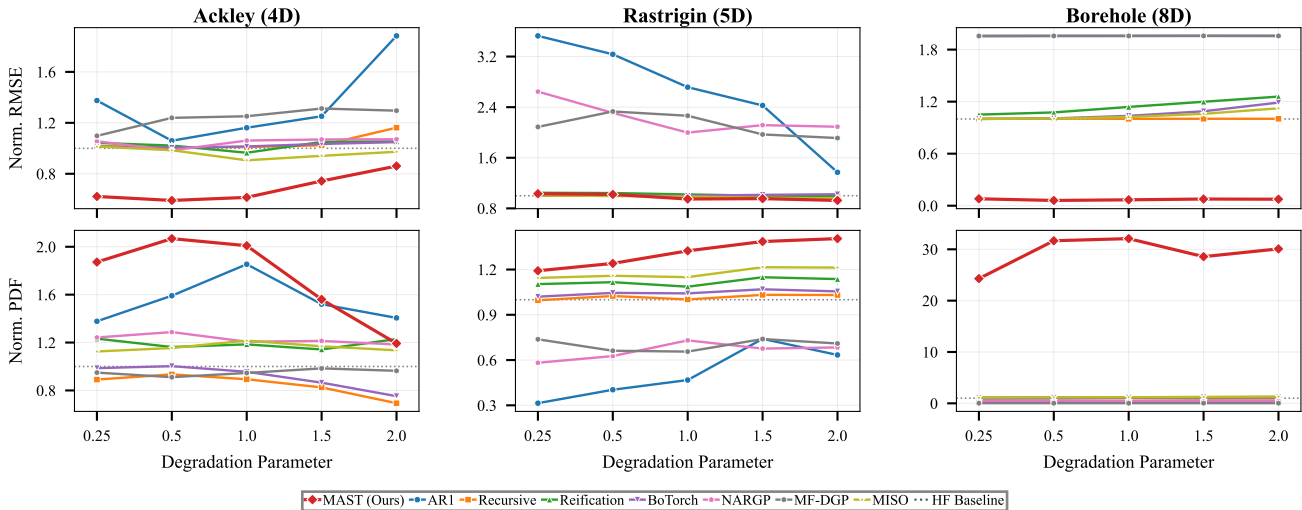


Figure 3. Sensitivity of surrogate model performance to fidelity discrepancy. The cost parameter d controls the deviation between low- and high-fidelity functions per Eq (17): low d yields high inter-fidelity correlation, while high d increases discrepancy. Top row: Normalized RMSE; bottom row: Normalized Mean PDF.

decoupling discrepancy correction from prediction fusion, MAST exploits this principle, reducing overconfident uncertainty estimates and preventing distant high-fidelity observations from exerting undue influence. This enables stable predictive behaviour under sparse budgets, weak or spatially varying fidelity relationships, and increasing dimensionality, adapting naturally as the relative fidelity gap changes—precisely the data-scarce settings where existing multi-fidelity surrogates deteriorate or become poorly calibrated. Notably, MAST achieves competitive or superior performance without requiring nested sampling designs, collocated observations, learned inter-fidelity correlations, global linear correlation assumptions, or complex

and expensive approximate inference. While expressive correlation-based models can be competitive when abundant multi-fidelity data are available, MAST provides a robust alternative across the full range of conditions. These findings suggest MAST is a practical default for expensive black-box problems where low-fidelity information is available but imperfect. Current limitations include the assumption of shared input dimensions across fidelities; future work will extend MAST to non-nested input spaces where high-fidelity models include additional variables. We are also developing an acquisition function for multi-fidelity Bayesian optimization that leverages MAST’s cost-aware weighting for joint fidelity and location selection.

Impact Statement

This work advances multi-fidelity surrogate modelling, a foundational technique for reducing computational costs in simulation-based engineering design and scientific computing. By enabling accurate predictions with fewer expensive high-fidelity evaluations, MAST can reduce the computational resources and energy consumption associated with complex simulations in aerospace, materials science, and other engineering domains. While surrogate modelling techniques are general-purpose and could theoretically be applied in harmful contexts, we see no direct ethical concerns specific to this work beyond those inherent to computational modelling research broadly. The primary societal benefit lies in reducing computational costs for simulation-based design, potentially enabling more thorough exploration of design spaces within fixed computational budgets.

References

- Alvarez, M. A. and Lawrence, N. D. Computationally efficient convolved multiple output Gaussian processes. *The Journal of Machine Learning Research*, 12:1459–1500, 2011.
- Alvarez, M. A., Rosasco, L., Lawrence, N. D., and others. Kernels for vector-valued functions: A review. *Foundations and Trends® in Machine Learning*, 4(3):195–266, 2012.
- Balandat, M., Karrer, B., Jiang, D., Daulton, S., Letham, B., Wilson, A. G., and Bakshy, E. BoTorch: A framework for efficient Monte-Carlo Bayesian optimization. *Advances in neural information processing systems*, 33: 21524–21538, 2020.
- Brevault, L., Balesdent, M., and Hebbal, A. Overview of Gaussian process based multi-fidelity techniques with variable relationship between fidelities, application to aerospace systems. *Aerospace Science and Technology*, 107:106339, 2020.
- Chung, H.-S. and Alonso, J. Using gradients to construct cokriging approximation models for high-dimensional design optimization problems. In *40th AIAA Aerospace Sciences Meeting & Exhibit*, pp. 317, 2002.
- Cutajar, K., Pullin, M., Damianou, A., Lawrence, N., and González, J. Deep Gaussian processes for multi-fidelity modeling. *arXiv preprint arXiv:1903.07320*, 2019.
- Ding, F. and Kareem, A. A multi-fidelity shape optimization via surrogate modeling for civil structures. *Journal of wind engineering and industrial aerodynamics*, 178:49–56, 2018.
- Do, B. and Zhang, R. MULTI-FIDELITY BAYESIAN OPTIMIZATION: A REVIEW. 12 2024. URL <http://arxiv.org/abs/2311.13050>.
- Fan, M., Yoon, B.-J., Dougherty, E., Alexander, F., Urban, N., Arróyave, R., and Qian, X. Multi-fidelity bayesian optimization with multiple information sources of input-dependent fidelity. In *The 40th Conference on Uncertainty in Artificial Intelligence*, 2024.
- Fernández-Godino, M. G. Review of multi-fidelity models. 5 2024. doi: 10.3934/acse.2023015. URL <http://arxiv.org/abs/1609.07196><http://dx.doi.org/10.3934/acse.2023015>.
- Forrester, A., Sobester, A., and Keane, A. *Engineering design via surrogate modelling: a practical guide*. John Wiley & Sons, 2008.
- Forrester, A. I., Sóbester, A., and Keane, A. J. Multi-fidelity optimization via surrogate modelling. *Proceedings of the Royal Society A: Mathematical, Physical and Engineering Sciences*, 463(2088):3251–3269, 12 2007. ISSN 14712946. doi: 10.1098/rspa.2007.1900.
- Ghoreishi, S. F. and Allaire, D. L. A fusion-based multi-information source optimization approach using knowledge gradient policies. In *2018 AIAA/ASCE/AHS/ASC Structures, Structural Dynamics, and Materials Conference*, pp. 1159, 2018.
- Han, Z. H. and Görtz, S. Hierarchical kriging model for variable-fidelity surrogate modeling. *AIAA Journal*, 50(9):1885–1896, 9 2012. ISSN 00011452. doi: 10.2514/1.J051354.
- Han, Z.-H., Görtz, S., and Zimmermann, R. Improving variable-fidelity surrogate modeling via gradient-enhanced kriging and a generalized hybrid bridge function. *Aerospace Science and technology*, 25(1):177–189, 2013.
- Kandasamy, K., Dasarathy, G., Schneider, J., and Póczos, B. Multi-fidelity Bayesian Optimisation with Continuous Approximations. Technical report, 2017.
- Keane, A. J. Cokriging for robust design optimization. *AIAA journal*, 50(11):2351–2364, 2012.
- Kennedy, M. C. and O’hagan, A. Predicting the Output from a Complex Computer Code When Fast Approximations Are Available. Technical Report 1, 2000. URL <https://about.jstor.org/terms>.
- Kim, J. Benchmark functions for bayesian optimization, 2020.

- Laguna, M. and Marti, R. Experimental testing of advanced scatter search designs for global optimization of multimodal functions. *Journal of Global Optimization*, 33(2): 235–255, 2005.
- Lam, R., Allaire, D., and Willcox, K. Multifidelity Optimization using Statistical Surrogate Modeling for Non-Hierarchical Information Sources. Technical report, 2015.
- Laurenceau, J. and Sagaut, P. Building efficient response surfaces of aerodynamic functions with kriging and cokriging. *AIAA journal*, 46(2):498–507, 2008.
- Le Gratiet, L. and Garnier, J. Recursive co-kriging model for design of computer experiments with multiple levels of fidelity. *International Journal for Uncertainty Quantification*, 4(5), 2014.
- Leary, S. J., Bhaskar, A., and Keane, A. J. A derivative based surrogate model for approximating and optimizing the output of an expensive computer simulation. *Journal of Global Optimization*, 30(1):39–58, 2004.
- Liu, H., Cai, J., and Ong, Y.-S. Remarks on multi-output Gaussian process regression. *Knowledge-Based Systems*, 144:102–121, 2018.
- Liu, X., Zhao, W., and Wan, D. Multi-fidelity Co-Kriging surrogate model for ship hull form optimization. *Ocean engineering*, 243:110239, 2022.
- Matar, C., Cinnella, P., and Gloerfelt, X. Cost-effective multi-fidelity strategy for the optimization of high-Reynolds number turbine flows guided by LES. *Aerospace Science and Technology*, pp. 110426, 2025.
- Mikkola, P., Martinelli, J., Filstroff, L., and Kaski, S. Multi-Fidelity Bayesian Optimization with Unreliable Information Sources. Technical report, 2023.
- Molga, M. and Smutnicki, C. Test functions for optimization needs. *Test functions for optimization needs*, 101(48):32, 2005.
- Morris, M. D. The Design and Analysis of Computer Experiments. *Journal of the American Statistical Association*, 99(468):1203–1204, 2004. doi: 10.1198/jasa.2004.s360. URL <https://doi.org/10.1198/jasa.2004.s360>.
- Morris, M. D., Mitchell, T. J., and Ylvisaker, D. Bayesian Design and Analysis of Computer Experiments: Use of Derivatives in Surface Prediction. *Technometrics*, 35(3): 243–255, 1993. doi: 10.1080/00401706.1993.10485320. URL <https://www.tandfonline.com/doi/abs/10.1080/00401706.1993.10485320>.
- Park, J. S. *Tuning Complex Computer Codes to Data and Optimal Designs*. PhD thesis, University of Illinois, Urbana-Champaign, 1 1991.
- Perdikaris, P., Venturi, D., Royset, J. O., and Karniadakis, G. E. Multi-fidelity modelling via recursive co-kriging and Gaussian–Markov random fields. *Proceedings of the Royal Society A: Mathematical, Physical and Engineering Sciences*, 471(2179):20150018, 2015.
- Perdikaris, P., Raissi, M., Damianou, A., Lawrence, N. D., and Karniadakis, G. E. Nonlinear information fusion algorithms for data-efficient multi-fidelity modelling. *Proceedings of the Royal Society A: Mathematical, Physical and Engineering Sciences*, 473(2198), 2 2017. ISSN 14712946. doi: 10.1098/rspa.2016.0751.
- Picheny, V., Wagner, T., and Ginsbourger, D. A benchmark of kriging-based infill criteria for noisy optimization. *Structural and multidisciplinary optimization*, 48 (3):607–626, 2013.
- Poloczek, M., Wang, J., and Frazier, P. Multi-information source optimization. *Advances in neural information processing systems*, 30, 2017.
- Rasmussen, C. E. and Williams, C. K. I. *Gaussian processes for machine learning*. MIT Press, 2006. ISBN 026218253X.
- Song, J., Chen, Y., and Yue, Y. A General Framework for Multi-fidelity Bayesian Optimization with Gaussian Processes. Technical report, 2019.
- Takeno, S., Fukuoka, H., Tsukada, Y., Koyama, T., Shiga, M., Takeuchi, I., and Karasuyama, M. Multi-fidelity Bayesian Optimization with Max-value Entropy Search and its Parallelization. Technical report, 2020.
- Thomison, W. D. and Allaire, D. A Model Reification Approach to Fusing Information from Multifidelity Information Sources. Technical report, 2017.
- Toal, D. J. Applications of multi-fidelity multi-output Kriging to engineering design optimization. *Structural and Multidisciplinary Optimization*, 66(6), 6 2023. ISSN 16151488. doi: 10.1007/s00158-023-03567-z.
- Toal, D. J. J. and Keane, A. J. Efficient multipoint aerodynamic design optimization via cokriging. *Journal of Aircraft*, 48(5):1685–1695, 2011.
- Vaiuso, A., Immordino, G., Righi, M., and Da Ronch, A. Multi-fidelity transonic aerodynamic loads estimation using Bayesian neural networks with transfer learning. *Aerospace Science and Technology*, 163, 8 2025. ISSN 12709638. doi: 10.1016/j.ast.2025.110301.

Wang, X., Jin, Y., Schmitt, S., and Olhofer, M. Recent Advances in Bayesian Optimization. *ACM Computing Surveys*, 55(13s), 12 2023. ISSN 15577341. doi: 10.1145/3582078.

Wiegand, M., Prots, A., Meyer, M., Schmidt, R., Voigt, M., and Mailach, R. Robust Design Optimization of a Compressor Rotor Using Recursive Cokriging Based Multi-Fidelity Uncertainty Quantification and Multi-Fidelity Optimization. *Journal of Turbomachinery*, 147(6):61009, 2025.

Wu, J., Toscano-Palmerin, S., Frazier, P. I., and Wilson, A. G. Practical multi-fidelity Bayesian optimization for hyperparameter tuning. In *Uncertainty in Artificial Intelligence*, pp. 788–798, 2020.

A. Benchmark Test Functions

This appendix provides detailed specifications for all benchmark functions used in the experimental evaluation. We first describe the cost-controlled multi-fidelity framework, then present each function with its mathematical formulation and discrepancy structure.

A.1. Cost-Controlled Multi-Fidelity Framework

All benchmark functions follow a unified degradation-controlled formulation that enables systematic variation of inter-fidelity correlation:

$$f_{\text{LF}}(\mathbf{x}) = f_{\text{HF}}(\mathbf{x}) + d \cdot \delta(\mathbf{x}), \quad (17)$$

where $d \geq 0$ is the degradation parameter controlling the degree of low-fidelity deviation, and $\delta(\mathbf{x})$ is a function-specific discrepancy term capturing the systematic bias between fidelity levels. This formulation has several desirable properties:

- When $d = 0$, the low-fidelity exactly matches the high-fidelity: $f_{\text{LF}} = f_{\text{HF}}$.
- Increasing d monotonically decreases inter-fidelity correlation.
- The discrepancy structure $\delta(\mathbf{x})$ can be spatially varying or constant depending on the function.

Unless otherwise noted, all two-fidelity experiments use $d = 1$. For three-fidelity experiments, the intermediate mid-fidelity level uses $d = 0.5$ and the low-fidelity uses $d = 1$, establishing a hierarchy where fidelity quality degrades with increasing d .

A.2. Discrepancy Type Classification

The benchmark functions exhibit different discrepancy structures, which we classify into four categories:

Spatially-varying discrepancy. The discrepancy $\delta(\mathbf{x})$ varies across the input domain, meaning the low-fidelity approximation quality differs by region. This is common in engineering applications where simplified models may be accurate in some operating regimes but not others.

Oscillatory discrepancy. The discrepancy takes the form $\delta(\mathbf{x}) = A \sin(\omega_1 x_1 + \omega_2 x_2)$, introducing periodic errors that challenge methods assuming smooth inter-fidelity relationships.

Linear scaling discrepancy. The discrepancy is a linear function of the high-fidelity response: $\delta(\mathbf{x}) = (\gamma - 1)f_{\text{HF}}(\mathbf{x}) + \beta$. This represents the classical autoregressive assumption where linear inter-fidelity correlation holds globally. Function: Park2.

Noise-only discrepancy. The discrepancy is identically zero: $\delta(\mathbf{x}) = 0$. Fidelity levels differ only in observation noise, testing a method's ability to appropriately weight data sources based on noise characteristics alone.

A.3. Branin (2D)

The Branin function (Forrester et al., 2008) is a classical 2D optimization benchmark with three global minima.

Domain: $x_1 \in [-5, 10]$, $x_2 \in [0, 15]$

High-fidelity:

$$f_{\text{HF}}(\mathbf{x}) = a(x_2 - bx_1^2 + cx_1 - r)^2 + s(1 - t)\cos(x_1) + s \quad (18)$$

with parameters $a = 1$, $b = \frac{5.1}{4\pi^2}$, $c = \frac{5}{\pi}$, $r = 6$, $s = 10$, $t = \frac{1}{8\pi}$.

Discrepancy term: Based on perturbing the b coefficient:

$$\delta(\mathbf{x}) = f_{\text{HF}}(\mathbf{x}; b' = b - 0.1) - f_{\text{HF}}(\mathbf{x}) \quad (19)$$

Global minima: $f(\mathbf{x}^*) \approx 0.398$ at $\mathbf{x}^* \in \{(-\pi, 12.275), (\pi, 2.275), (9.425, 2.475)\}$

A.4. Rosenbrock (nD , $n \geq 2$)

A variant of the classic Rosenbrock valley function (Molga & Smutnicki, 2005; Lam et al., 2015) with an oscillatory low-fidelity component.

Domain: $\mathbf{x} \in [-5, 10]^n$

High-fidelity:

$$f_{\text{HF}}(\mathbf{x}) = \sum_{i=1}^{n-1} [100(x_{i+1} - x_i^2)^2 + (1 - x_i)^2] \quad (20)$$

Discrepancy term:

$$\delta(\mathbf{x}) = A \sin(\omega_1 x_1 + \omega_2 x_2) \quad (21)$$

with default parameters $A = 0.1$, $\omega_1 = 10$, $\omega_2 = 5$.

Global minimum: $f(1) = 0$

A.5. Rastrigin (nD)

A highly multimodal function commonly used for testing global optimization algorithms (Molga & Smutnicki, 2005).

Domain: $\mathbf{x} \in [-5.12, 5.12]^n$

High-fidelity:

$$f_{\text{HF}}(\mathbf{x}) = An + \sum_{i=1}^n [x_i^2 - A \cos(2\pi x_i)] \quad (22)$$

with $A = 10$.

Discrepancy term:

$$\delta(\mathbf{x}) = A \sin(\omega_1 x_1 + \omega_2 x_2) \quad (23)$$

with default parameters $A = 0.1$, $\omega_1 = 10$, $\omega_2 = 5$.

Global minimum: $f(0) = 0$

A.6. Ackley (nD)

A widely-used multimodal function with many local minima surrounding a global minimum at the origin (Molga & Smutnicki, 2005).

Domain: $\mathbf{x} \in [-5, 5]^n$

High-fidelity:

$$f_{\text{HF}}(\mathbf{x}) = -a \exp \left(-b \sqrt{\frac{1}{n} \sum_{i=1}^n x_i^2} \right) - \exp \left(\frac{1}{n} \sum_{i=1}^n \cos(cx_i) \right) + a + e \quad (24)$$

with parameters $a = 20$, $b = 0.2$, $c = 2\pi$, and $e = \exp(1)$.

Discrepancy term:

$$\delta(\mathbf{x}) = 0 \quad (25)$$

The low-fidelity differs from high-fidelity only through observation noise levels.

Global minimum: $f(0) = 0$

A.7. Levy (nD)

A multimodal function with sinusoidal components (Laguna & Marti, 2005).

Domain: $\mathbf{x} \in [-10, 10]^n$

High-fidelity:

$$f_{\text{HF}}(\mathbf{x}) = \sin^2(\pi w_1) + \sum_{i=1}^{n-1} (w_i - 1)^2 [1 + 10 \sin^2(\pi w_i + 1)] + (w_n - 1)^2 [1 + \sin^2(2\pi w_n)] \quad (26)$$

where $w_i = 1 + \frac{x_i - 1}{4}$.

Discrepancy term:

$$\delta(\mathbf{x}) = A \sin(\omega_1 x_1 + \omega_2 x_2) \quad (27)$$

with default parameters $A = 0.1, \omega_1 = 10, \omega_2 = 5$.

Global minimum: $f(1) = 0$

A.8. Hartmann3 (3D)

A 3D function with four local minima, commonly used for testing global optimization (Kim, 2020).

Domain: $\mathbf{x} \in [0, 1]^3$

High-fidelity:

$$f_{\text{HF}}(\mathbf{x}) = \sum_{i=1}^4 \alpha_i \exp\left(-\sum_{j=1}^3 A_{ij}(x_j - P_{ij})^2\right) \quad (28)$$

with parameters:

$$\alpha = (1.0, 1.2, 3.0, 3.2)^\top$$

$$\mathbf{A} = \begin{pmatrix} 3.0 & 10.0 & 30.0 \\ 0.1 & 10.0 & 35.0 \\ 3.0 & 10.0 & 30.0 \\ 0.1 & 10.0 & 35.0 \end{pmatrix}, \quad \mathbf{P} = \begin{pmatrix} 0.3689 & 0.1170 & 0.2673 \\ 0.4699 & 0.4387 & 0.7470 \\ 0.1091 & 0.8732 & 0.5547 \\ 0.0381 & 0.5743 & 0.8828 \end{pmatrix}$$

Discrepancy term: Based on perturbing the α vector:

$$\delta(\mathbf{x}) = f_{\text{HF}}(\mathbf{x}; \alpha + \Delta\alpha) - f_{\text{HF}}(\mathbf{x}) \quad (29)$$

with $\Delta\alpha = (0.01, -0.01, -0.1, 0.1)^\top$.

A.9. Hartmann6 (6D)

A 6D extension of the Hartmann function with four local minima (Picheny et al., 2013).

Domain: $\mathbf{x} \in [0, 1]^6$

High-fidelity:

$$f_{\text{HF}}(\mathbf{x}) = \sum_{i=1}^4 \alpha_i \exp\left(-\sum_{j=1}^6 A_{ij}(x_j - P_{ij})^2\right) \quad (30)$$

with parameters:

$$\alpha = (1.0, 1.2, 3.0, 3.2)^\top$$

$$\mathbf{A} = \begin{pmatrix} 10.0 & 3.0 & 17.0 & 3.5 & 1.7 & 8.0 \\ 0.05 & 10.0 & 17.0 & 0.1 & 8.0 & 14.0 \\ 3.0 & 3.5 & 1.7 & 10.0 & 17.0 & 8.0 \\ 17.0 & 8.0 & 0.05 & 10.0 & 0.1 & 14.0 \end{pmatrix}$$

$$\mathbf{P} = 10^{-4} \times \begin{pmatrix} 1312 & 1696 & 5569 & 124 & 8283 & 5886 \\ 2329 & 4135 & 8307 & 3736 & 1004 & 9991 \\ 2348 & 1451 & 3522 & 2883 & 3047 & 6650 \\ 4047 & 8828 & 8732 & 5743 & 1091 & 381 \end{pmatrix}$$

Discrepancy term: Same perturbation as Hartmann3:

$$\delta(\mathbf{x}) = f_{\text{HF}}(\mathbf{x}; \boldsymbol{\alpha} + \Delta\boldsymbol{\alpha}) - f_{\text{HF}}(\mathbf{x}) \quad (31)$$

with $\Delta\boldsymbol{\alpha} = (0.01, -0.01, -0.1, 0.1)^\top$.

A.10. Park1 (4D)

The first Park function with a combination of rational and exponential terms (Park, 1991).

Domain: $\mathbf{x} \in [0, 1]^4$

High-fidelity:

$$f_{\text{HF}}(\mathbf{x}) = \frac{x_1}{2} \left(\sqrt{1 + (x_2 + x_3^2) \frac{x_4}{x_1^2}} - 1 \right) + (x_1 + 3x_4) \exp(1 + \sin(x_3)) \quad (32)$$

Discrepancy term:

$$\delta(\mathbf{x}) = \frac{\sin(x_1)}{10} \cdot f_{\text{HF}}(\mathbf{x}) - 2x_1 + x_2^2 + x_3^2 + 0.5 \quad (33)$$

A.11. Park2 (4D)

The second Park function with exponential and trigonometric terms (Park, 1991).

Domain: $\mathbf{x} \in [0, 1]^4$

High-fidelity:

$$f_{\text{HF}}(\mathbf{x}) = \frac{2}{3} \exp(x_1 + x_2) - x_4 \sin(x_3) + x_3 \quad (34)$$

Discrepancy term:

$$\delta(\mathbf{x}) = (\gamma - 1)f_{\text{HF}}(\mathbf{x}) + \beta \quad (35)$$

with default parameters $\gamma = 1.2$ and $\beta = -1.0$.

Low-fidelity (at $d = 1$):

$$f_{\text{LF}}(\mathbf{x}) = \gamma \cdot f_{\text{HF}}(\mathbf{x}) + \beta \quad (36)$$

A.12. Borehole (8D)

A physics-based function modelling water flow rate through a borehole (Morris et al., 1993). This function has practical significance in groundwater modelling.

Domain and physical parameters:

Variable	Description	Lower	Upper
r_w	Borehole radius (m)	0.05	0.15
r	Radius of influence (m)	100	50,000
T_u	Upper aquifer transmissivity (m ² /yr)	63,070	115,600
H_u	Upper aquifer potentiometric head (m)	990	1,110
T_l	Lower aquifer transmissivity (m ² /yr)	63.1	116
H_l	Lower aquifer potentiometric head (m)	700	820
L	Borehole length (m)	1,120	1,680
K_w	Borehole hydraulic conductivity (m/yr)	9,855	12,045

High-fidelity:

$$f_{\text{HF}}(\mathbf{x}) = \frac{2\pi T_u (H_u - H_l)}{\ln(r/r_w) \left(1 + \frac{2LT_u}{\ln(r/r_w) \cdot r_w^2 K_w} + \frac{T_u}{T_l} \right)} \quad (37)$$

Discrepancy term: Based on coefficient simplifications:

$$\delta(\mathbf{x}) = \frac{5T_u(H_u - H_l)}{\ln(r/r_w) \left(1.5 + \frac{2LT_u}{\ln(r/r_w) \cdot r_w^2 K_w} + \frac{T_u}{T_l} \right)} - f_{\text{HF}}(\mathbf{x}) \tag{38}$$

The low-fidelity uses coefficient 5 instead of $2\pi \approx 6.28$ and 1.5 instead of 1 in the denominator.

A.13. Summary Table

Table 3 summarizes all benchmark functions used in this study.

Table 3. Summary of benchmark test functions.

Function	Dim.	Domain	Discrepancy Type
Branin	2	$[-5, 10] \times [0, 15]$	Coefficient perturbation
Rosenbrock	n	$[-5, 10]^n$	Oscillatory
Rastrigin	n	$[-5.12, 5.12]^n$	Oscillatory
Ackley	n	$[-5, 5]^n$	Noise only
Levy	n	$[-10, 10]^n$	Oscillatory
Hartmann3	3	$[0, 1]^3$	Parameter perturbation
Hartmann6	6	$[0, 1]^6$	Parameter perturbation
Park1	4	$[0, 1]^4$	Multiplicative + polynomial
Park2	4	$[0, 1]^4$	Linear scaling + offset
Borehole	8	Physical bounds	Coefficient simplification

B. Extended Sensitivity Analysis Results

This appendix presents complete sensitivity analysis results across all benchmark functions for three experimental configurations: budget allocation (Section B.1), total budget scaling (Section B.2), and fidelity discrepancy (Section B.3). The three representative functions shown in the main text (Ackley, Rastrigin, Borehole) were selected to span different dimensionalities and discrepancy structures; here we report results for all ten benchmark functions to demonstrate the generality of our findings.

B.1. Sensitivity to Budget Allocation

Figures 4–7 show normalized RMSE and Mean PDF as the HF cost fraction varies with total budget fixed at $\mathcal{B} = 5D$.

On the low-dimensional functions (Figure 4), MAST maintains stable RMSE performance across all budget allocations, achieving consistent improvement over the baseline. On Hartmann3, where AR1 excels due to strong global linear correlation, MAST remains competitive across allocations. The uncertainty quantification results show MAST providing well-calibrated predictions throughout, while some others exhibits characteristic instability with large PDF spikes at certain allocations.

For the mid-dimensional functions (Figure 5), MAST demonstrates robust performance regardless of budget split. On Park2, where the inter-fidelity relationship is a simple linear scaling, AR1 achieves strong results, but MAST maintains competitive performance without requiring knowledge of this structure. The deep learning approaches (NARGP, MF-DGP) consistently underperform the baseline across all allocations on these functions.

The higher-dimensional results (Figures 6–7) reveal MAST’s key advantage in maintaining strong performance as dimensionality increases across all allocations with exceptional uncertainty calibration. MAST consistently outperforms all competitors regardless of budget split. Notably, at extreme allocations (HF fraction = 0.1 or 0.9), competing methods show degradation or instability while MAST remains robust, demonstrating its insensitivity to suboptimal allocation decisions.

B.2. Sensitivity to Total Budget

Figures 8–11 show normalized performance as total budget scales with fixed 70%/30% HF/LF resources allocation.

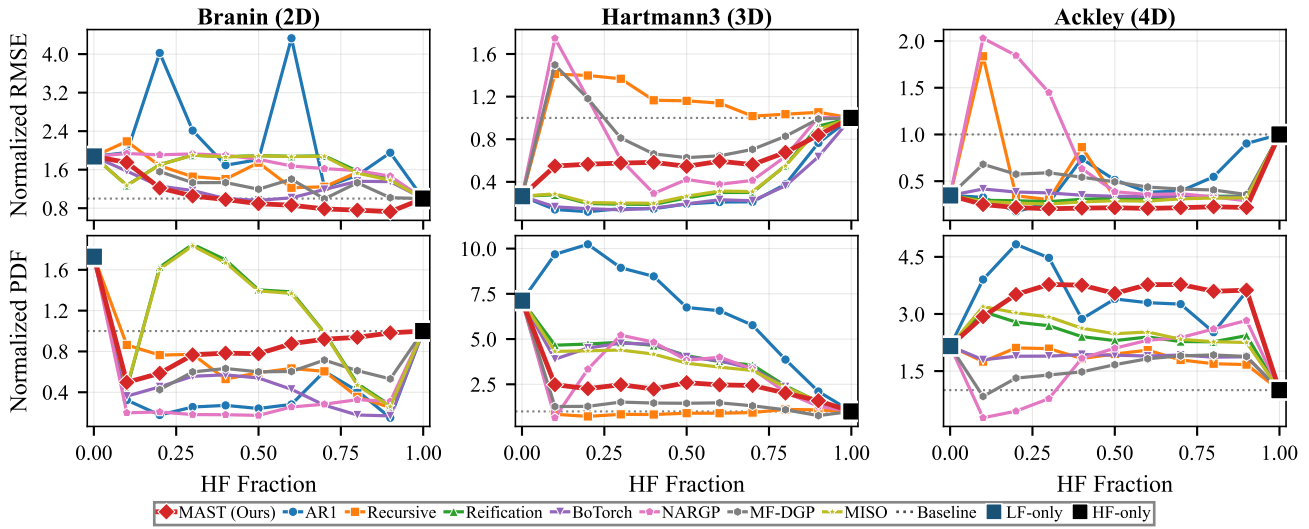


Figure 4. Budget allocation sensitivity for low-dimensional functions: Branin (2D), Hartmann3 (3D), and Ackley (4D).

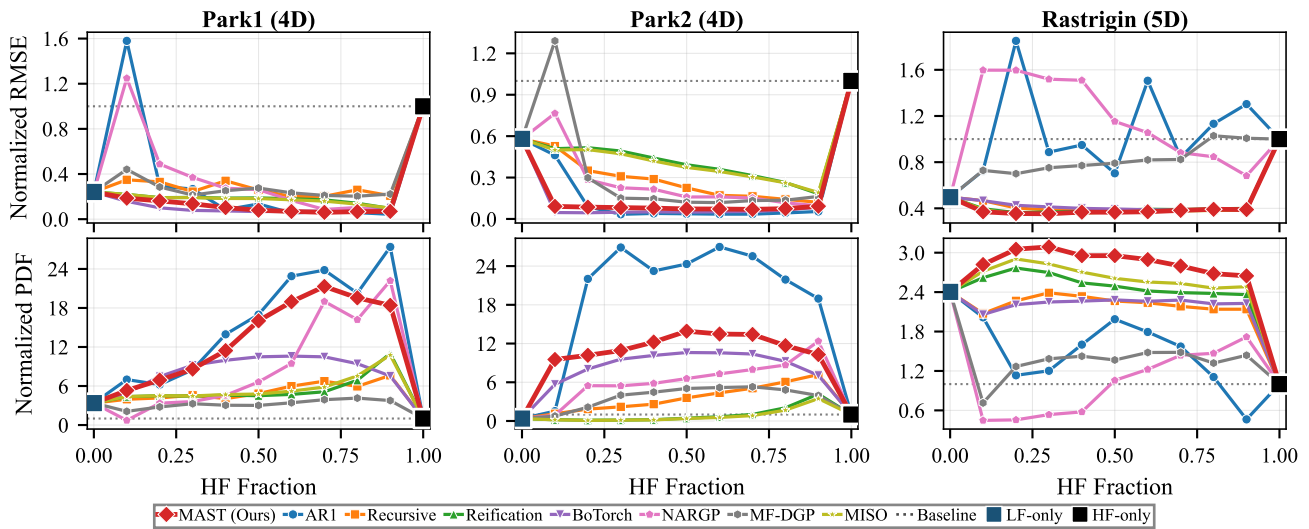


Figure 5. Budget allocation sensitivity for mid-dimensional functions: Park1 (4D), Park2 (4D), and Rastrigin (5D).

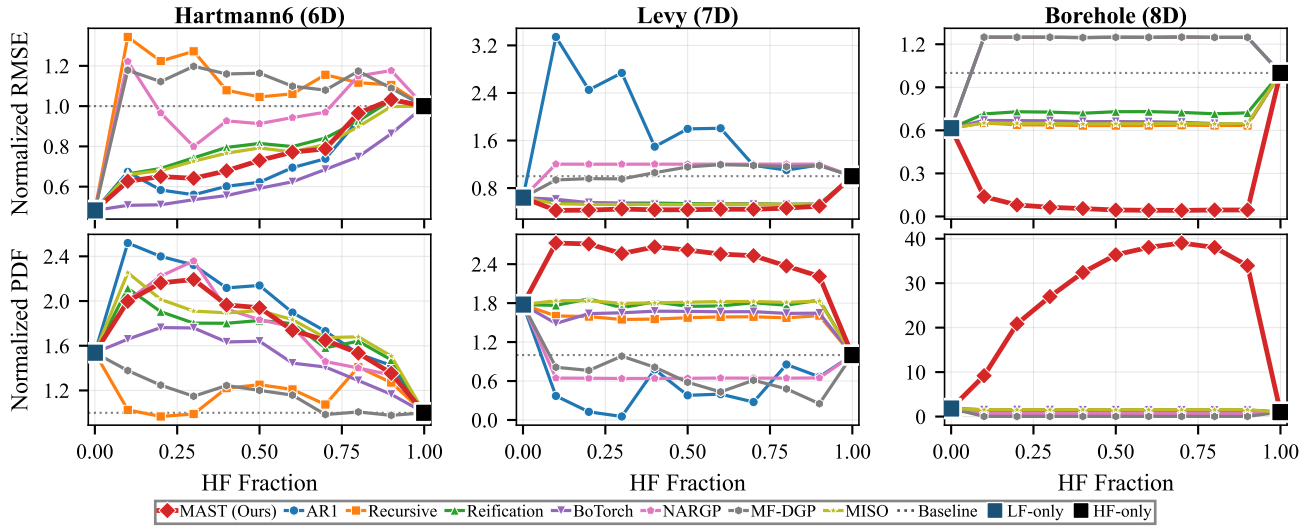


Figure 6. Budget allocation sensitivity for higher-dimensional functions: Hartmann6 (6D), Levy (7D), and Borehole (8D).

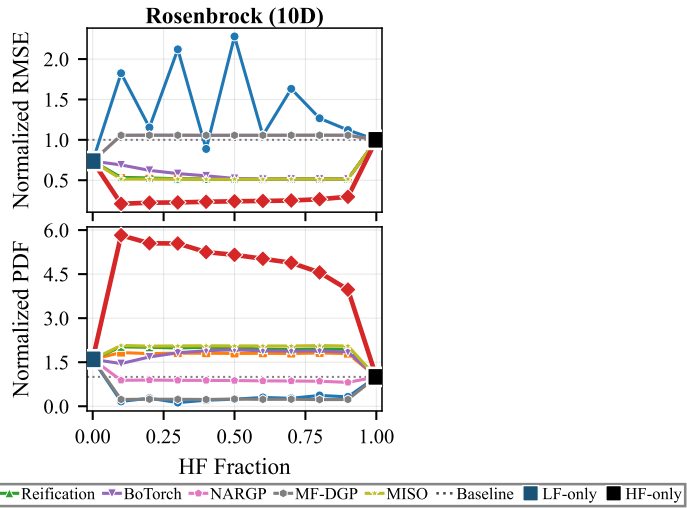


Figure 7. Budget allocation sensitivity for Rosenbrock (10D).

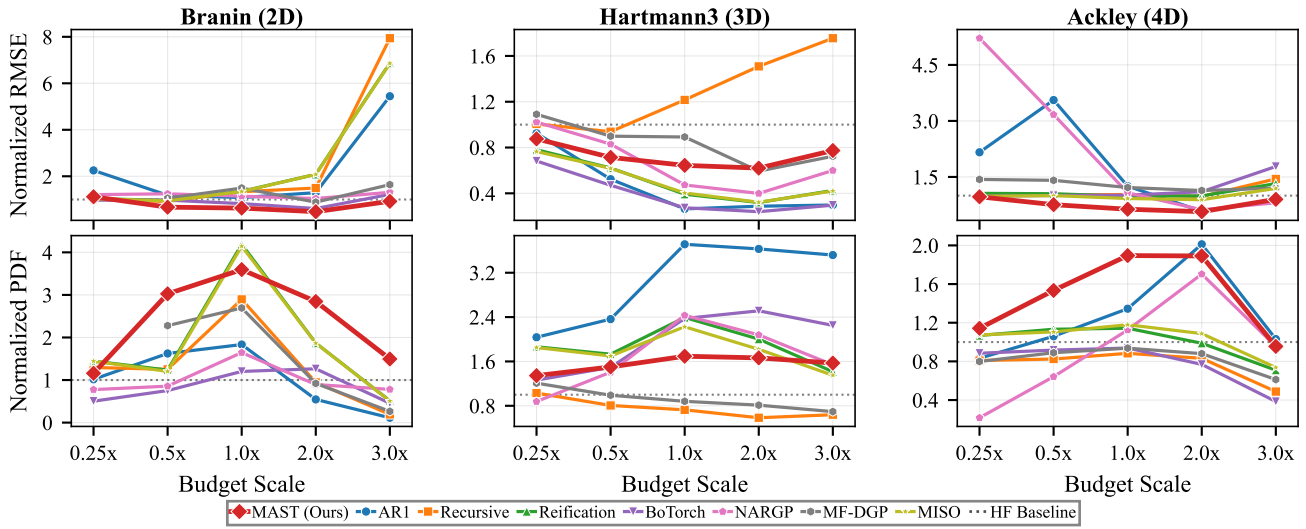


Figure 8. Budget scaling sensitivity for low-dimensional functions: Branin (2D), Hartmann3 (3D), and Ackley (4D).

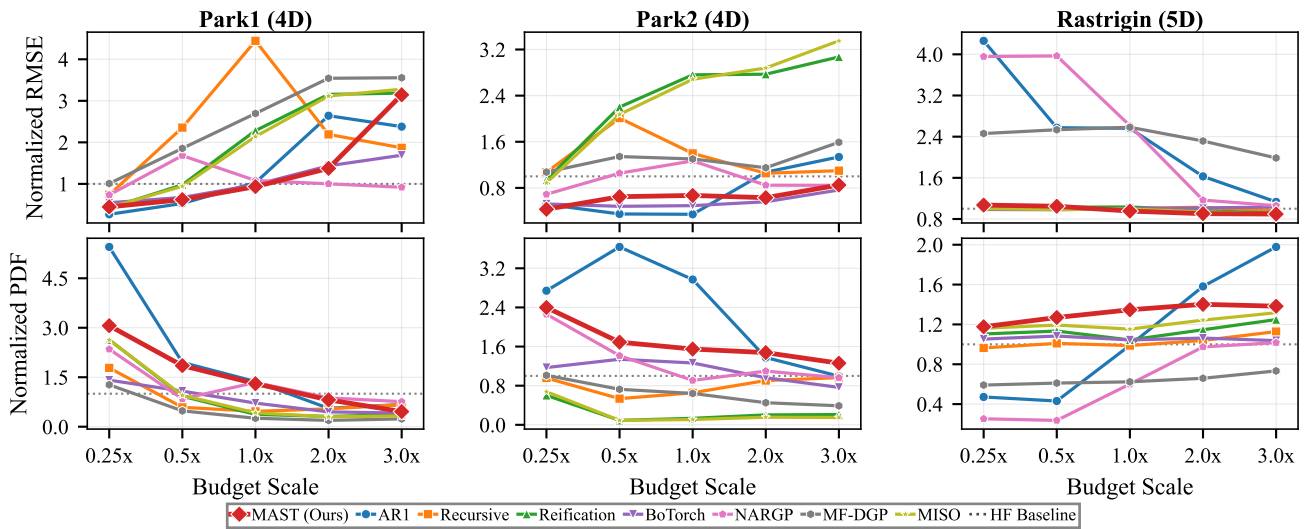


Figure 9. Budget scaling sensitivity for mid-dimensional functions: Park1 (4D), Park2 (4D), and Rastrigin (5D).

On low-dimensional functions (Figure 8), MAST demonstrates stable performance across all budget scales. On Branin, MAST maintains consistent RMSE improvement from the smallest to largest budget, while AR1 shows high variance. On Hartmann3, both MAST and AR1 achieve good performance, with AR1 benefiting from the function’s amenable correlation structure. On Ackley, several methods (AR1, Recursive) exhibit problematic scaling behavior with performance degrading as budget increases, a counterintuitive result where more data leads to worse predictions, likely due to numerical instabilities.

For mid-dimensional functions (Figure 9), the data-hungry nature of deep multi-fidelity methods becomes apparent. On Rastrigin for instance, NARGP and MF-DGP improve substantially as budget increases from $0.25\times$ to $3.0\times$, but even at triple budget they fail to match MAST’s performance at the smallest budget allocation. This confirms that expressive models require substantially more data to realize their potential, limiting applicability in expensive-to-evaluate settings.

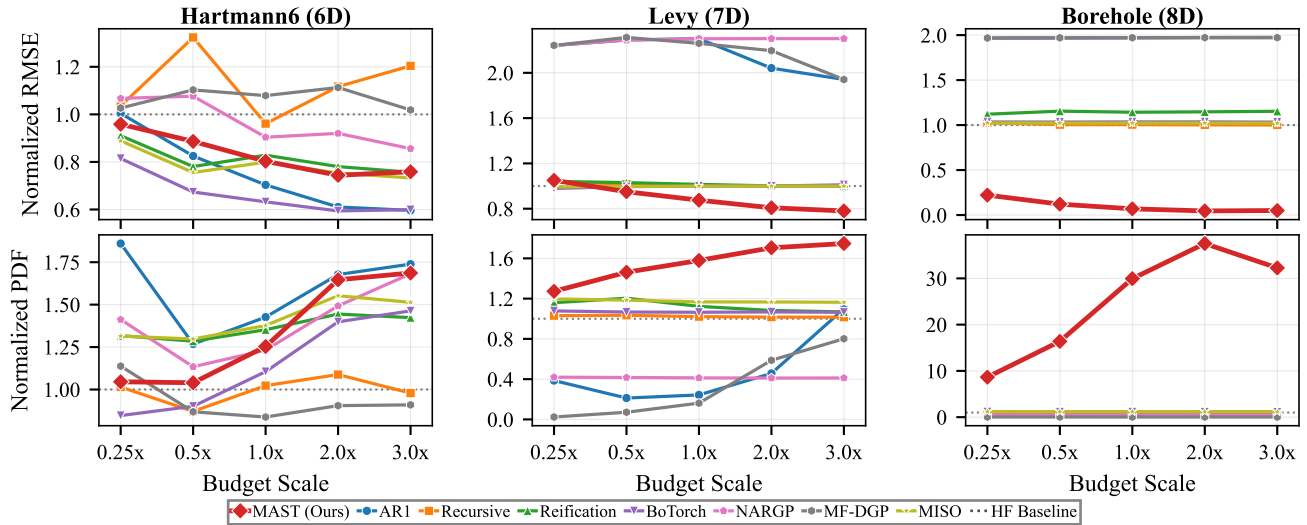


Figure 10. Budget scaling sensitivity for higher-dimensional functions: Hartmann6 (6D), Levy (7D), and Borehole (8D).

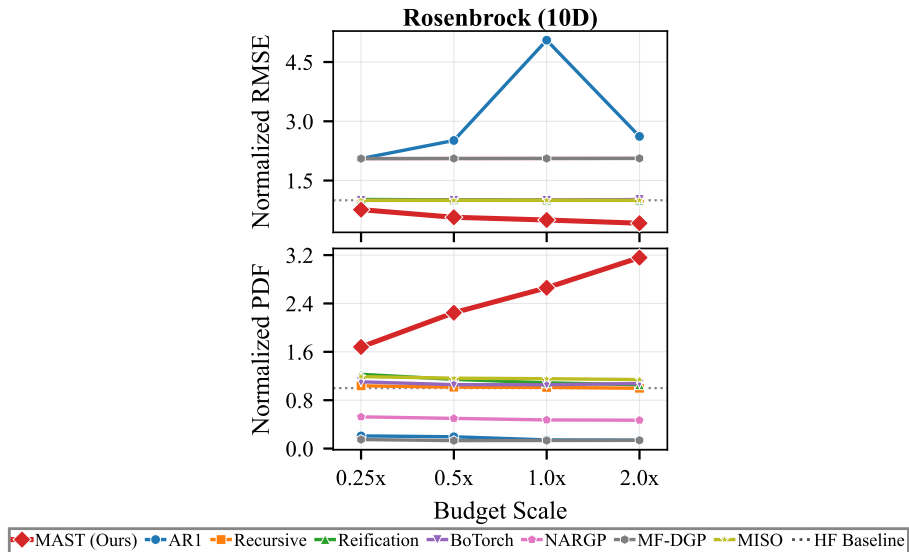


Figure 11. Budget scaling sensitivity for Rosenbrock (10D).

The higher-dimensional results (Figures 10–11) highlight MAST’s suitability for budget-constrained applications. MAST maintains a significant RMSE reduction from the smallest to largest budget with exceptional uncertainty calibration, while MF-DGP in some instances, exhibits near-zero PDF across all budgets indicating severely miscalibrated uncertainty estimates. On Rosenbrock (10D), MAST achieves consistent improvement while AR1 degrades catastrophically as budget

increases. These results underscore that MAST’s geometric inductive bias provides stable performance precisely in the data-scarce regimes where competing methods become unreliable.

B.3. Sensitivity to Fidelity Discrepancy

Figures 12–15 show normalized performance as the degradation parameter d in Equation (17) varies from 0.25 (high inter-fidelity correlation) to 2.0 (low correlation).

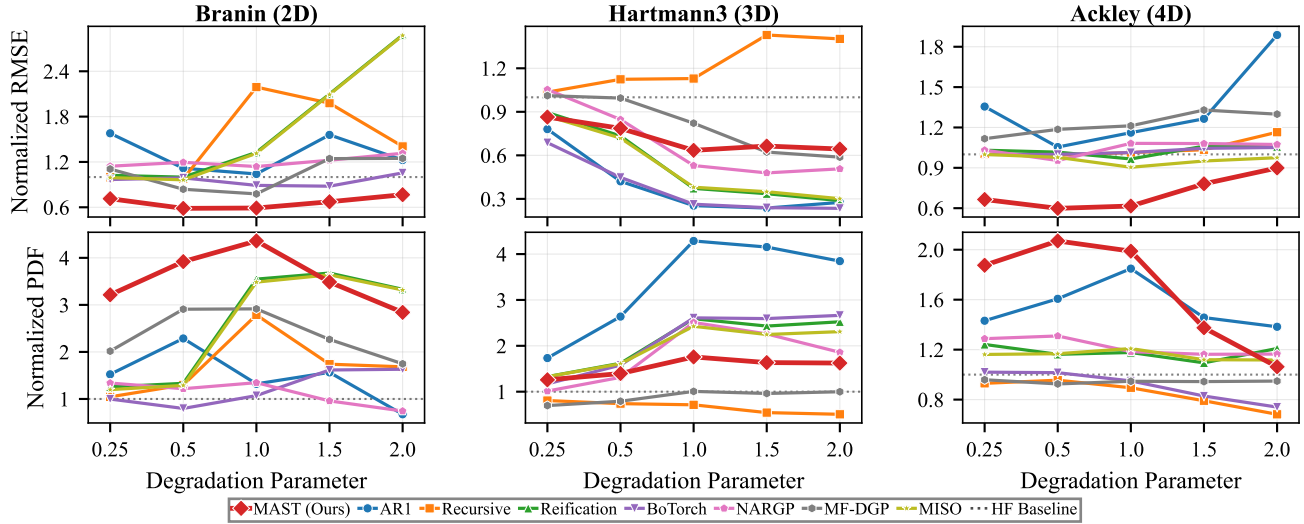


Figure 12. Fidelity discrepancy sensitivity for low-dimensional functions: Branin (2D), Hartmann3 (3D), and Ackley (4D).

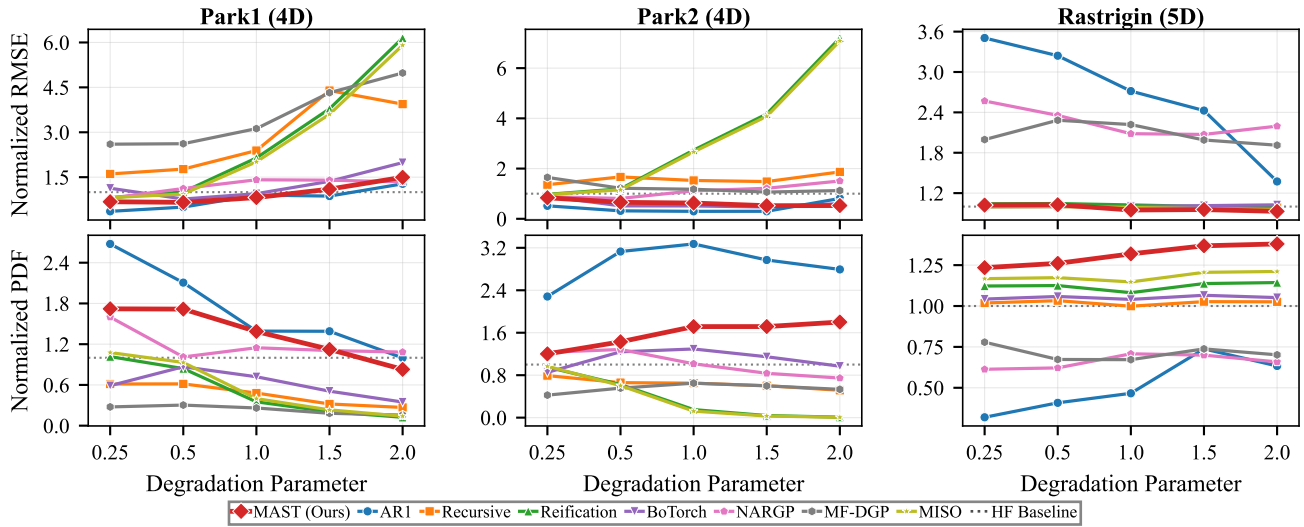


Figure 13. Fidelity discrepancy sensitivity for mid-dimensional functions: Park1 (4D), Park2 (4D), and Rastrigin (5D).

On low-dimensional functions (Figure 12), MAST maintains consistent RMSE improvement across the entire range of fidelity discrepancies. MAST achieves stable performance regardless of whether the low-fidelity closely approximates the high-fidelity ($d = 0.25$) or deviates substantially ($d = 2.0$). On Hartmann3, ARI performs well at low discrepancy but its advantage diminishes as d increases, while MAST remains stable throughout. The uncertainty quantification results show MAST providing well-calibrated predictions across all discrepancy levels.

For mid-dimensional functions (Figure 13), MAST demonstrates graceful adaptation to varying fidelity gaps. On Rastrigin, ARI shows severe degradation as discrepancy increases, eventually performing $3\times$ worse than baseline, while MAST maintains consistent improvement. On Park1 and Park2, most methods hover near baseline regardless of discrepancy level,

failing to leverage low-fidelity information even when correlation is high while MAST extracts value across the full range.

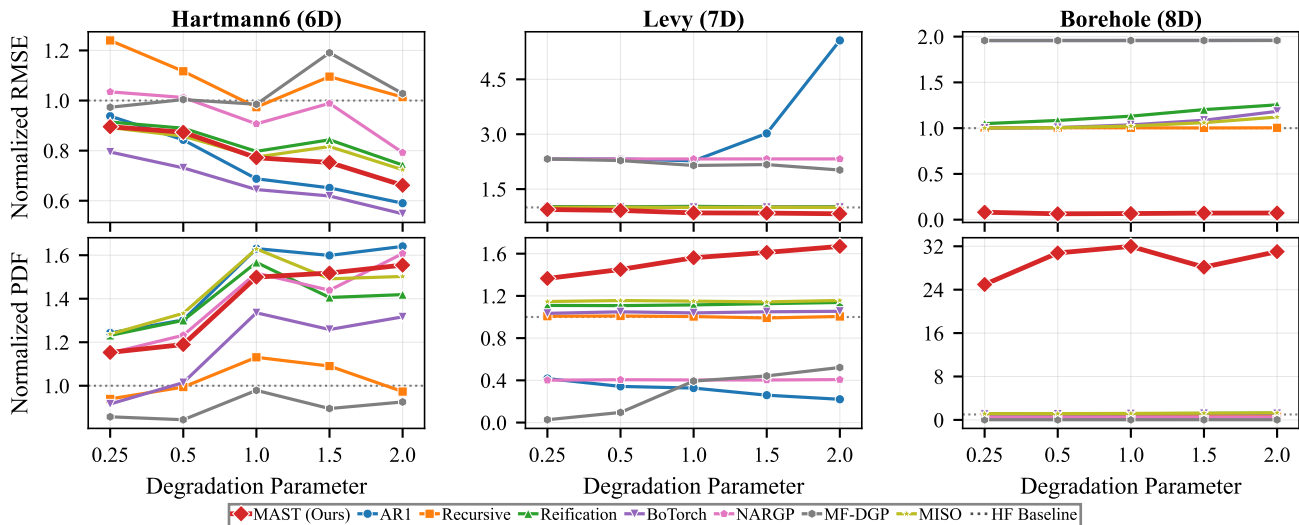


Figure 14. Fidelity discrepancy sensitivity for higher-dimensional functions: Hartmann6 (6D), Levy (7D), and Borehole (8D).

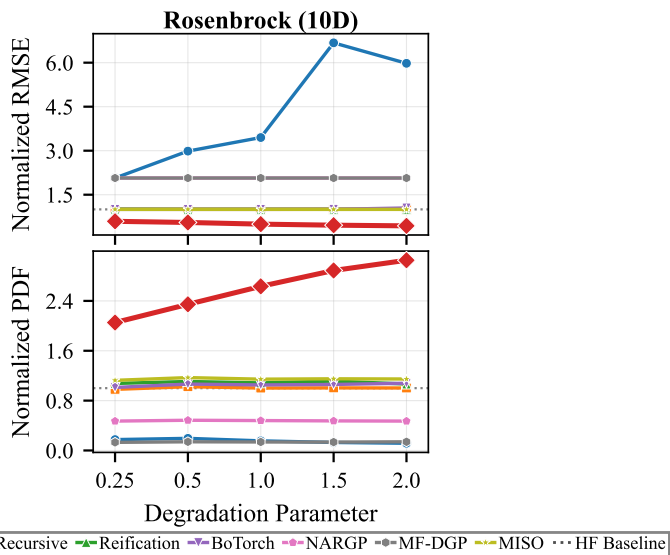


Figure 15. Fidelity discrepancy sensitivity for Rosenbrock (10D).

The higher-dimensional results (Figures 14–15) demonstrate MAST’s robustness to varying inter-fidelity relationships. On Borehole, MAST achieves exceptional performance across all discrepancy levels, while MF-DGP exhibits persistent miscalibration regardless of correlation strength. On Levy and Rosenbrock, MAST maintains stable improvement while competing methods either hover near baseline (BoTorch, MISO, Recursive) or degrade substantially (AR1, NARGP). Crucially, MAST achieves this robustness by explicitly encoding the fidelity gap through its cost-aware weighting exponent rather than learning correlations that may not generalize—adapting naturally as the relative fidelity gap changes.

C. Extended Methodology

This appendix provides a comprehensive description of the MAST algorithm, including the complete pseudocode and detailed implementation considerations for each stage. Algorithm 1 in the main text provides a compact summary; here we present the full procedure with additional detail.

C.1. Complete Algorithm

Algorithm 1 MAST: Multi-fidelity Augmented Surrogate with Trust-region Weighting (Extended)

Require: Data $\{\mathcal{D}_m\}_{m=1}^M$; Cost ratios $C_m = \mathcal{C}_M/\mathcal{C}_m$ for $m < M$

Ensure: Trained surrogate model \mathcal{M}

- 1: **Stage 1: Train independent GPs**
- 2: Normalise all inputs to $[0, 1]^D$
- 3: **for** $m = 1$ to M **do**
- 4: Train \mathcal{GP}_m on $\mathcal{D}_m \rightarrow$ obtain learned noise $\hat{\sigma}_m$
- 5: **end for**
- 6: **Stage 2: Augment lower-fidelity data toward highest fidelity**
- 7: **for** $m = 1$ to $M - 1$ **do**
- 8: *Fit discrepancy GP*
- 9: **for** $j = 1$ to N_M **do**
- 10: $\delta_j \leftarrow y_j^{(M)} - \mu_m(\mathbf{x}_j^{(M)})$ {Residuals at HF locations}
- 11: **end for**
- 12: Train \mathcal{GP}_{δ_m} on $\{(\mathbf{x}_j^{(M)}, \delta_j)\}_{j=1}^{N_M}$
- 13: *Correct and blend each point*
- 14: Compute cost-based exponent: $\alpha_m \leftarrow \frac{\log_{10}(C_m)}{2}$
- 15: **for** $i = 1$ to N_m **do**
- 16: $\mu_{\delta_m}^{(i)}, \sigma_{\delta_m}^{2(i)} \leftarrow \mathcal{GP}_{\delta_m}(\mathbf{x}_i^{(m)})$ {Discrepancy prediction}
- 17: $\mu_M^{(i)}, \sigma_M^{2(i)} \leftarrow \mathcal{GP}_M(\mathbf{x}_i^{(m)})$ {HF prediction}
- 18: **for** $j = 1$ to N_M **do**
- 19: $d_{ij} \leftarrow \|\tilde{\mathbf{x}}_i^{(m)} - \tilde{\mathbf{x}}_j^{(M)}\|_2$
- 20: **end for**
- 21: $r_i \leftarrow g(\min_j d_{ij})$ {Trust region radius, e.g., $g(d) = \sqrt{d}$ }
- 22: $\mathcal{N}_i \leftarrow \{j : d_{ij} \leq r_i\}$ {Local neighbours}
- 23: **for** $j \in \mathcal{N}_i$ **do**
- 24: $w_j \leftarrow h(d_{ij}; \alpha_m)$ {Distance weight, e.g., $h(d; \alpha) = 1 - d^\alpha$ }
- 25: **end for**
- 26: $W_m^{(i)} \leftarrow 1 - \frac{1}{|\mathcal{N}_i|} \sum_{j \in \mathcal{N}_i} w_j$
- 27: $\tilde{y}_i^{(m)} \leftarrow W_m^{(i)} \cdot \left(y_i^{(m)} + \mu_{\delta_m}^{(i)} \right) + (1 - W_m^{(i)}) \cdot \mu_M^{(i)}$ {Eq. (11)}
- 28: $\tilde{\sigma}_i^2 \leftarrow \left(W_m^{(i)} \right)^2 \left(\hat{\sigma}_m^2 + \sigma_{\delta_m}^{2(i)} \right) + \left(1 - W_m^{(i)} \right)^2 \sigma_M^{2(i)}$ {Eq. (12)}
- 29: **end for**
- 30: **end for**
- 31: **Stage 3: Train fusion GP with fixed observation variances**
- 32: $\mathcal{D}_{\text{aug}} \leftarrow \{(\mathbf{x}_j^{(M)}, y_j^{(M)}, \hat{\sigma}_M^2)\}_{j=1}^{N_M} \cup \bigcup_{m=1}^{M-1} \{(\mathbf{x}_i^{(m)}, \tilde{y}_i, \tilde{\sigma}_i^2)\}_{i=1}^{N_m}$
- 33: Train \mathcal{GP} on \mathcal{D}_{aug} with fixed per-point noise variances
- 34: **return** $\mathcal{M} \leftarrow \mathcal{GP}$

C.2. Stage 1: Independent Baseline Modelling

The first stage establishes independent Gaussian process models for each fidelity level to capture their intrinsic characteristics and estimate observation noise levels.

Input normalisation. All input coordinates are normalised to the unit hypercube $[0, 1]^D$ using the domain bounds. For each dimension d and input \mathbf{x} :

$$\tilde{x}_d = \frac{x_d - x_d^{\min}}{x_d^{\max} - x_d^{\min}}, \quad (39)$$

where x_d^{\min} and x_d^{\max} are the lower and upper bounds of the d -th input dimension. This normalisation ensures that distances computed in Stage 2 are comparable across dimensions and that the trust region radius scales appropriately.

GP training. For each fidelity level $m \in \{1, \dots, M\}$, we fit an independent Gaussian process with a squared exponential (RBF) kernel with automatic relevance determination (ARD):

$$k_m(\mathbf{x}, \mathbf{x}') = \sigma_{f,m}^2 \exp\left(-\frac{1}{2} \sum_{d=1}^D \frac{(x_d - x'_d)^2}{\ell_{m,d}^2}\right), \quad (40)$$

where $\sigma_{f,m}^2$ is the output variance and $\ell_m = (\ell_{m,1}, \dots, \ell_{m,D})$ are the per-dimension lengthscales. The hyperparameters $\{\ell_m, \sigma_{f,m}^2, \sigma_m^2\}$ are estimated via Type-II maximum likelihood estimation (MLE), maximising the log marginal likelihood:

$$\log p(\mathbf{y}_m | \mathbf{X}_m, \boldsymbol{\theta}_m) = -\frac{1}{2} \mathbf{y}_m^\top \mathbf{K}_m^{-1} \mathbf{y}_m - \frac{1}{2} \log |\mathbf{K}_m| - \frac{N_m}{2} \log(2\pi), \quad (41)$$

where $\mathbf{K}_m = \mathbf{K}_{mm} + \sigma_m^2 \mathbf{I}$ is the regularised covariance matrix. The learned noise variance $\hat{\sigma}_m^2$ serves as an estimate of the intrinsic measurement uncertainty at fidelity level m .

C.3. Stage 2: Discrepancy Modelling and Spatially-Weighted Augmentation

The second stage transforms each lower-fidelity dataset into an augmented dataset by (i) learning the discrepancy between fidelities, (ii) computing spatially-adaptive weights, and (iii) blending corrected low-fidelity values with high-fidelity predictions.

C.3.1. DISCREPANCY MODELLING

For each fidelity level $m < M$, we model the discrepancy $\delta_m(\mathbf{x}) = f_M(\mathbf{x}) - f_m(\mathbf{x})$ by fitting a GP to residuals computed at the high-fidelity observation locations.

Residual computation. Using the trained fidelity- m GP, we predict at each high-fidelity location and compute residuals:

$$\delta_j = y_j^{(M)} - \mu_m(\mathbf{x}_j^{(M)}), \quad j = 1, \dots, N_M, \quad (42)$$

where $\mu_m(\cdot)$ is the posterior mean of \mathcal{GP}_m . These residuals capture the systematic bias between fidelity levels at the high-fidelity observation locations.

Discrepancy GP. We fit a Gaussian process \mathcal{GP}_{δ_m} to the residual dataset $\{(\mathbf{x}_j^{(M)}, \delta_j)\}_{j=1}^{N_M}$, again using an RBF kernel with ARD lengthscales. This yields posterior predictions $\mu_{\delta_m}(\mathbf{x})$ and $\sigma_{\delta_m}^2(\mathbf{x})$ at any location \mathbf{x} , representing the expected discrepancy and its uncertainty.

C.3.2. SPATIALLY-ADAPTIVE WEIGHTING

The weighting mechanism determines how much to trust the corrected low-fidelity value versus the high-fidelity GP prediction at each low-fidelity location. The key insight is that this trust should depend on spatial proximity to high-fidelity calibration data.

Distance computation. For each low-fidelity point $\mathbf{x}_i^{(m)}$, we compute the Euclidean distance to all high-fidelity points in the normalised input space:

$$d_{ij} = \|\tilde{\mathbf{x}}_i^{(m)} - \tilde{\mathbf{x}}_j^{(M)}\|_2, \quad j = 1, \dots, N_M. \quad (43)$$

Adaptive trust region. A naive approach would aggregate contributions from all high-fidelity points, but this leads to problematic behaviour: a low-fidelity point with a nearby high-fidelity neighbour would still be influenced by distant high-fidelity observations elsewhere in the domain, artificially inflating the high-fidelity weight. To ensure that only *locally relevant* high-fidelity information contributes, we introduce an adaptive trust region based on an N -sphere centred at $\mathbf{x}_i^{(m)}$.

The trust region radius is defined as a function of the minimum distance to any high-fidelity point:

$$r_i = g(d_{\min}), \quad \text{where} \quad d_{\min} = \min_j d_{ij}. \quad (44)$$

In principle, any monotonically increasing function $g : \mathbb{R}^+ \rightarrow \mathbb{R}^+$ can be used. This flexibility allows practitioners to adapt the trust region behaviour to domain-specific requirements. In this work, we adopt:

$$g(d) = \sqrt{d}, \quad (45)$$

which we found empirically to provide robust performance across our benchmark suite. The square-root scaling ensures that the trust region expands sub-linearly with distance, providing a balance between local sensitivity and spatial coverage. Only high-fidelity points within this N -sphere contribute to the weight computation:

$$\mathcal{N}_i = \{j : d_{ij} \leq r_i\}. \quad (46)$$

By construction, the nearest high-fidelity point is always included in \mathcal{N}_i (since $d_{\min} \leq r_i = \sqrt{d_{\min}}$ for $d_{\min} \leq 1$ in the normalised space).

Distance-based weights. For each high-fidelity point $j \in \mathcal{N}_i$, we compute a distance-based weight. In general, this weight should be a decreasing function of distance, modulated by the fidelity cost ratio:

$$w_j = h(d_{ij}; \alpha_m), \quad (47)$$

where $h : \mathbb{R}^+ \times \mathbb{R}^+ \rightarrow [0, 1]$ is any function that is monotonically decreasing in its first argument (distance) and α_m is a fidelity-dependent exponent derived from the cost ratio. Alternative formulations are possible, including exponential decay $h(d; \alpha) = \exp(-\alpha d)$ or inverse-distance weighting $h(d; \alpha) = 1/(1 + d^\alpha)$. In this work, we adopt:

$$h(d; \alpha) = 1 - d^\alpha, \quad \text{where} \quad \alpha_m = \frac{\log_{10}(C_m)}{2}, \quad (48)$$

which we found to work well empirically. The exponent α_m is determined by the cost ratio $C_m = C_M/C_m$, encoding the economic hierarchy of fidelity levels. When high-fidelity evaluations are substantially more expensive (large C_m), α_m increases and the weight decay becomes more gradual, extending the spatial influence of high-fidelity observations commensurate with their acquisition cost.

The individual weights are aggregated into a single low-fidelity weight:

$$W_m^{(i)} = 1 - \frac{1}{|\mathcal{N}_i|} \sum_{j \in \mathcal{N}_i} w_j. \quad (49)$$

By construction, $W_m^{(i)} \rightarrow 0$ when the low-fidelity point is very close to high-fidelity observations (favouring the high-fidelity prediction), and $W_m^{(i)} \rightarrow 1$ when distant (favouring the corrected low-fidelity value).

C.3.3. AUGMENTED OBSERVATIONS AND VARIANCE PROPAGATION

Blended mean. Each low-fidelity observation is first corrected by adding the predicted discrepancy, then blended with the high-fidelity GP prediction:

$$\tilde{y}_i^{(m)} = W_m^{(i)} \cdot \underbrace{\left(y_i^{(m)} + \mu_{\delta_m}(\mathbf{x}_i^{(m)}) \right)}_{\text{corrected LF value}} + (1 - W_m^{(i)}) \cdot \underbrace{\mu_M(\mathbf{x}_i^{(m)})}_{\text{HF prediction}}. \quad (50)$$

Variance propagation. The augmented observation $\tilde{y}_i^{(m)}$ is a weighted sum of two independent quantities. The corrected low-fidelity value has variance $\hat{\sigma}_m^2 + \sigma_{\delta_m}^2(\mathbf{x}_i^{(m)})$, combining the original observation noise with the uncertainty in the discrepancy prediction. The high-fidelity component contributes variance $\sigma_M^2(\mathbf{x}_i^{(m)})$ from the GP posterior. Since these components are independent, the total variance follows from standard propagation rules:

$$\tilde{\sigma}_i^2 = \left(W_m^{(i)} \right)^2 \left(\hat{\sigma}_m^2 + \sigma_{\delta_m}^2(\mathbf{x}_i^{(m)}) \right) + \left(1 - W_m^{(i)} \right)^2 \sigma_M^2(\mathbf{x}_i^{(m)}). \quad (51)$$

This formulation ensures appropriate uncertainty quantification: augmented points near high-fidelity data inherit lower uncertainty from the high-fidelity predictions, while points far from high-fidelity observations retain higher uncertainty reflecting the extrapolated nature of the discrepancy correction.

C.4. Stage 3: Heteroscedastic GP Fusion

The final stage trains a single Gaussian process on the combined dataset consisting of original high-fidelity observations and augmented lower-fidelity observations from all levels:

$$\mathcal{D}_{\text{aug}} = \left\{ (\mathbf{x}_j^{(M)}, y_j^{(M)}, \hat{\sigma}_M^2) \right\}_{j=1}^{N_M} \bigcup_{m=1}^{M-1} \left\{ (\mathbf{x}_i^{(m)}, \tilde{y}_i^{(m)}, \tilde{\sigma}_i^2) \right\}_{i=1}^{N_m}. \quad (52)$$

Fixed heteroscedastic noise. Crucially, the per-point noise variances $\{\hat{\sigma}_M^2, \tilde{\sigma}_i^2\}$ are *fixed* during GP training—they are not treated as learnable hyperparameters. This design choice has several advantages:

1. It avoids the numerical instabilities associated with jointly optimising heteroscedastic noise models.
2. It allows the GP to weight observations according to their pre-determined reliability, naturally down-weighting uncertain augmented points.
3. It preserves the uncertainty information propagated from Stage 2.

Only the kernel hyperparameters (lengthscales and output variance) are optimised via maximum likelihood estimation.

Prediction. At test time, the trained heteroscedastic GP provides posterior predictions $\mu(\mathbf{x}_*)$ and $\sigma^2(\mathbf{x}_*)$ that integrate information from all fidelity levels, with contributions weighted by both spatial proximity (via the kernel) and observation reliability (via the fixed noise variances).

C.5. Extension to Multiple Fidelity Levels

For $M > 2$ fidelity levels, MAST processes each lower-fidelity level independently toward the highest fidelity. This *parallel* augmentation strategy differs from the *sequential* approach used by recursive methods (e.g., recursive co-kriging), where fidelity m is modelled conditional on fidelity $m - 1$. The parallel approach has two advantages: (i) it avoids error accumulation across the fidelity hierarchy, and (ii) it allows each fidelity level to be calibrated directly against the target high-fidelity function.

C.6. Computational Complexity

The computational cost of MAST is dominated by GP training operations:

- **Stage 1:** Training M independent GPs with complexity $\mathcal{O}(N_m^3)$ each.
- **Stage 2:** For each fidelity $m < M$: training one discrepancy GP with $\mathcal{O}(N_M^3)$ complexity, plus $\mathcal{O}(N_m \cdot N_M)$ distance computations.
- **Stage 3:** Training one heteroscedastic GP with $\mathcal{O}(N_{\text{total}}^3)$ complexity, where $N_{\text{total}} = \sum_{m=1}^M N_m$.

The overall complexity is comparable to other GP-based multi-fidelity methods, with the main overhead being the discrepancy GP training and distance computations in Stage 2, which scale linearly with the number of fidelity levels.